

Lattice-QCD validation of hadron mass and trace-anomaly decomposition sum rules

Dennis Bollweg,¹ Heng-Tong Ding,² Xiang Gao,^{3,*} Ran Luo,^{2,†} and Swagato Mukherjee³

¹*Scientific Computing Core, Flatiron Institute, New York, New York 10010, USA*

²*Key Laboratory of Quark & Lepton Physics (MOE) and Institute of Particle Physics, Central China Normal University, Wuhan 430079, China*

³*Physics Department, Brookhaven National Laboratory, Upton, New York 11973, USA*

(Dated: January 21, 2026)

Abstract

We present the first lattice-QCD validation of multiple sum rules associated with quark–gluon decomposition of hadron mass by computing all components from first principles. We achieve this through nonperturbative renormalization of the QCD energy–momentum tensor, including its trace, in a gradient-flow scheme, followed by continuum extrapolations, two-loop matching to the $\overline{\text{MS}}$ scheme, and zero-flow-time extrapolations. These ingredients enable a direct and simultaneous verification, in a common renormalization scheme and scale, of multiple energy-density-based and trace-based mass decomposition sum rules proposed in the literature. We demonstrate the framework for the η_c and J/ψ charmonia using three fine lattice spacings with a physical strange-quark and near-physical up- and down-quark masses. We present the first lattice-QCD results for the gravitational form factor \bar{C} . We find sizable gluonic contributions to charmonia masses at the hadronic scale, $\sim 15\%$ in the Lorcé and Metz–Pasquini–Rodini decompositions. The trace-anomaly contribution in the Ji sum rule is $\sim 6\%$, while the gluonic component of the trace anomaly in the Hatta–Rajan–Tanaka sum rule is $\sim 35\%$. The method is general and can be straightforwardly adopted for lattice-QCD calculations of mass and spin decompositions as well as gravitational form factors of other hadrons and nuclei.

* xgao@bnl.gov

† ranluo@mails.ccnu.edu.cn

I. INTRODUCTION

The mass of nearly all visible matter in the Universe arises from asymptotic bound states of Quantum Chromodynamics (QCD) [1–3]. Quarks and gluons—almost massless at the Lagrangian level—form massive hadrons through strong, nonperturbative dynamics. Because of color confinement, partons are never observed in isolation, and how their confined dynamics generate hadron masses remains a fundamental question.

The QCD energy–momentum tensor (EMT) provides the field-theoretic bridge between quark–gluon degrees of freedom and hadronic observables. Its hadronic matrix elements relate the hadron mass to quark and gluon energies, explicit quark-mass terms, and the trace anomaly [4–8]. Gauge-invariant mass decompositions and the associated trace- and energy-density sum rules quantify this connection [9–15]. These sum rules state that the hadron mass equals the sum of all quark and gluon contributions, providing a concrete benchmark for how confined partons collectively generate mass.

To test these theoretical relations, two complementary approaches are essential: experimental access to EMT form factors and nonperturbative theoretical determination of EMT matrix elements. Experimentally, the 12 GeV program at Thomas Jefferson National Accelerator Facility and the forthcoming Electron–Ion Collider aim to probe gravitational form factors (GFFs) through deeply virtual exclusive processes, providing leading-twist information on the traceless EMT and its spatial structure [16–25]. However, only limited combinations of EMT components can be reconstructed, and the trace part governing the anomaly contribution remains inaccessible at leading twist.

A complete picture therefore requires first-principles information on all EMT components, including those beyond experimental reach. Lattice QCD offers a gauge-invariant, systematically improvable, nonperturbative framework to address this question. However, the reduction of the continuum rotational to the lattice hypercubic symmetry induces mixing of the EMT trace with power-divergent lower-dimensional operators [26, 27]. Additionally, conventional nonperturbative renormalization of lattice EMT using RI/MOM-type schemes are gauge dependent, infrared sensitive, and statistically noisy. As a result, past studies have largely been restricted to selected traceless components [28–40], with the trace-related component inferred using the relevant sum rules [7, 11, 41–45].

We overcome these challenges and provide the first direct lattice-QCD validation of hadron mass decompositions and the trace-anomaly sum rules by computing each of their constituent components. We employ nonperturbative renormalization of both traceless and trace parts of the EMT in the gradient-flow scheme, followed by continuum limit [46–49], two-loop matching to $\overline{\text{MS}}$ and zero-flow-time extrapolations [50–53]. This enables a consistent determination of all EMT components in a common scheme and scale, allowing a direct and simultaneous consistency check of multiple energy-density- and trace-based decompositions proposed in the literature [7–15].

II. $\overline{\text{MS}}$ -RENORMALIZED EMT VIA GRADIENT FLOW

The symmetric QCD EMT in Euclidean formulation, related to its Minkowski counterpart by the Wick rotation $[T_{\rho\sigma}]_M = i^{\delta_{t\rho} + \delta_{t\sigma}} [T_{\rho\sigma}]_E$, is

$$T_{\rho\sigma}(x) = \mathcal{O}_{1,\rho\sigma}(x) - \frac{1}{4}\mathcal{O}_{2,\rho\sigma}(x) + \frac{1}{4}\mathcal{O}_{3,\rho\sigma}(x) - \frac{1}{2}\mathcal{O}_{4,\rho\sigma}(x) - \mathcal{O}_{5,\rho\sigma}(x), \quad (1)$$

where,

$$\begin{aligned}
\mathcal{O}_{1,\rho\sigma} &= \frac{2}{g_0^2} \text{Tr}^c [F_{\rho\omega} F_{\sigma\omega}] , \\
\mathcal{O}_{2,\rho\sigma} &= \frac{2}{g_0^2} \delta_{\rho\sigma} \text{Tr}^c [F_{\omega\xi} F_{\omega\xi}] , \\
\mathcal{O}_{3,\rho\sigma} &= \sum_f \mathcal{O}_{3,\rho\sigma,f} = \sum_f \bar{\psi}_f \left(\gamma_\rho \overset{\leftrightarrow}{D}_\sigma + \gamma_\sigma \overset{\leftrightarrow}{D}_\rho \right) \psi_f , \\
\mathcal{O}_{4,\rho\sigma} &= \delta_{\rho\sigma} \sum_f \bar{\psi}_f \overset{\leftrightarrow}{D} \psi_f , \quad \mathcal{O}_{5,\rho\sigma} = \delta_{\rho\sigma} \sum_f m_f \bar{\psi}_f \psi_f .
\end{aligned} \tag{2}$$

Here, g_0 is the bare coupling, m_f the bare quark mass, Tr^c denotes the color trace, f labels quark flavors, and the covariant derivative is $\overset{\leftrightarrow}{D}_\rho = \vec{D}_\rho - \overset{\leftarrow}{D}_\rho$. For analyzing hadron mass decompositions, the EMT is separated into quark and gluon parts [54–56],

$$\begin{aligned}
T_{\rho\sigma} &= \sum_{X=q,g} T_{X,\rho\sigma} , \quad \text{with} \quad T_{q,\rho\sigma} = \frac{1}{4} \sum_{\mathbf{x}} \mathcal{O}_{3,\rho\sigma}(x) , \\
T_{g,\rho\sigma} &= \sum_{\mathbf{x}} \left[\mathcal{O}_{1,\rho\sigma}(x) - \frac{1}{4} \mathcal{O}_{2,\rho\sigma}(x) \right] .
\end{aligned} \tag{3}$$

The total EMT is conserved and hence does not require renormalization, but the individual components $T_{X,\rho\sigma}$ and $\mathcal{O}_{i,\rho\sigma}$ must be renormalized and mix under renormalization. Since renormalization and taking traces do not commute [7, 12, 57], must be renormalized first before taking its trace, which is essential for a consistent comparison of different mass decomposition formulations. The QCD equations of motion (EoM) imply $2\langle \mathcal{O}_{5,\rho\sigma,f} \rangle = -\langle \mathcal{O}_{4,\rho\sigma,f} \rangle$, where angular brackets denote matrix elements in a physical state.

The gradient flow [46–49] alleviates the problem of power-divergent mixing of lattice EMT [26, 27] by evolving lattice fields along a fictitious flow time t_f , which smooths ultraviolet fluctuations and renders composite operators finite at nonzero t_f . The flowed operators $\tilde{\mathcal{O}}_{i,\rho\sigma}(t_f, x)$ are nonperturbatively renormalized in the gradient-flow scheme at flow scale t_f , providing a common operator basis for evaluating distinct mass decomposition sum rules on equal footing. Their continuum limits are obtained by extrapolating results at several lattice spacings, $a \rightarrow 0$. The continuum-extrapolated $\tilde{\mathcal{O}}_{i,\rho\sigma}(t_f, x)$ are then matched to the $\overline{\text{MS}}$ scheme at scale μ using perturbatively known coefficients $\mathcal{O}_i^{\overline{\text{MS}}}(\mu) = M_{ij}(t_f, \mu) \tilde{\mathcal{O}}_j(t_f) + O(t_f)$, with $i, j = 1, 2, 3, 4$, valid for $2t_f \mu^2 \sim 1$ [50–52, 58]. The residual $O(t_f)$ corrections are finally removed by extrapolating $t_f \rightarrow 0$.

III. LATTICE QCD COMPUTATIONS

We use three 2+1-flavor HISQ gauge ensembles generated by the HotQCD Collaboration [59–61]. The light sea-quark masses correspond to a pion mass of about 160 MeV, and the strange sea-quark mass is tuned to its physical value. The ensembles span three lattice spacings, $a = 0.06, 0.05$, and 0.04 fm, with respective lattice sizes 64×48^3 , 64^4 , and 64^4 . For the valence charm we employ the set up of Refs. [62–77]—a tree-level

tadpole-improved Wilson–clover action, where the gauge links entering the Dirac and clover operators are 1-step HYP smeared [78].

We compute the η_c ($\Gamma = \gamma_5$) and J/ψ ($\Gamma = \gamma_{1,2,3}$) two-point correlation functions, $C_{\Gamma}^{2\text{pt}}(t) = \sum_{\mathbf{x}} \langle \mathcal{O}_{\Gamma}(\mathbf{x}, t) \mathcal{O}_{\Gamma}^{\dagger}(\mathbf{0}, 0) \rangle$, using Gaussian-smeared sources and sinks, and meson interpolating operators $\mathcal{O}_{\Gamma}(\mathbf{x}, t) = \bar{c}(\mathbf{x}, t) \Gamma c(\mathbf{x}, t)$. The valence charm-quark mass is tuned to reproduce the physical masses of η_c and J/ψ at the percent level.

Lattice gauge fields are evolved using the Zeuthen-flow discretization [79] and the fermion flow is implemented with a covariant Laplacian consistent with the valence action. Both flows are integrated with a third-order Runge–Kutta scheme [80], yielding $\mathcal{O}(a^2)$ flow-time discretization effects. Measurements are performed at $t_f = n \epsilon_f$ with $\epsilon_f = 5.1984 \times 10^{-4} \text{ fm}^2$, for integers n spanning the window used in our continuum and $t_f \rightarrow 0$ extrapolations. We use clover discretization to construct the flowed operator $\tilde{\mathcal{O}}_{1,\rho\sigma}(t_f)$, and its trace $\tilde{\mathcal{O}}_{2,\rho\sigma}(t_f)$, for the flowed gauge fields. For the flowed operator $\tilde{\mathcal{O}}_{3,\rho\sigma}(t_f)$, and its trace $\tilde{\mathcal{O}}_{4,\rho\sigma}(t_f)$, we employ “ringed” fermion fields [51] to cancel wave–function renormalization.

Vacuum-subtracted hadronic matrix elements of flowed operators, $\langle H | \tilde{\mathcal{O}}_{i,\rho\sigma} | H \rangle(\mu)$ with $H = \eta_c, J/\psi$, are extracted from the three-point function $C_{\Gamma}^{\rho\sigma}(t, \tau) = \sum_{\mathbf{x}, \mathbf{y}} \langle \mathcal{O}_{\Gamma}(\mathbf{x}, t) \tilde{\mathcal{O}}_{i,\rho\sigma}(\mathbf{y}, \tau) \mathcal{O}_{\Gamma}^{\dagger}(\mathbf{0}, 0) \rangle - \langle C_{\Gamma}^{2\text{pt}}(t) \rangle \sum_{\mathbf{y}} \langle \tilde{\mathcal{O}}_{i,\rho\sigma}(\mathbf{y}, \tau) \rangle$, using source–sink separations $t/a = 22, 24, 26, 28, 30$, and 32 . Keeping our focus on hadron mass decompositions we only consider hadrons at rest. The Quark-line-connected three-point functions for $\tilde{\mathcal{O}}_{3,\rho\sigma}$ and $\tilde{\mathcal{O}}_{4,\rho\sigma}$ are computed using standard sequential-source methods. While computing the disconnected three-point functions for $\tilde{\mathcal{O}}_{1,\rho\sigma}$ and $\tilde{\mathcal{O}}_{2,\rho\sigma}$ we use the all-mode averaging (AMA) [81] technique for the corresponding the two-point correlation functions to improve statistical precision. The quark-line-disconnected contributions of the charm quark to $\tilde{\mathcal{O}}_{3,\rho\sigma}$ and $\tilde{\mathcal{O}}_{4,\rho\sigma}$ are found to be negligible. We neglect all light-flavor (up, down, strange) contributions entering solely through quark-line-disconnected diagrams for the charmonia states. As we shall see later, all sum rules are satisfied without these contributions, showing these contributions are, indeed, negligible compared to our present precision.

We fit the spectral decomposition of the ratio $R_{\Gamma}^{\rho\sigma}(t, \tau) = C_{\Gamma}^{\rho\sigma}(t, \tau) / C_{\Gamma}^{2\text{pt}}(t)$ at each t_f using two-exponential ansatz to obtain the EMT matrix elements of η_c and J/ψ in the limit $t \rightarrow \infty$. We also employ summation fits, where $R_{\Gamma}^{\rho\sigma}(t, \tau)$ are summed over the operator insertion time τ and extrapolated to $t \rightarrow \infty$ through a linear fit in $1/t$. These complementary methods yield consistent results across ensembles and flow times, providing confidence that excited-state effects due to finite source–sink separations of the three-point functions are under control.

IV. HADRONIC MATRIX ELEMENTS OF $\overline{\text{MS}}$ -RENORMALIZED EMT

These procedures provide hadronic matrix elements of component $\tilde{\mathcal{O}}_{i,\rho\sigma}$, nonperturbatively renormalized in the gradient-flow scheme at multiple flow times t_f and for three lattice spacings. To obtain matrix elements of $\tilde{\mathcal{O}}_{i,\rho\sigma}$ renormalized in the $\overline{\text{MS}}$ scheme at $\mu = 2 \text{ GeV}$, we perform three sequential steps: (i) continuum, $a \rightarrow 0$, extrapolations of the gradient-flow–renormalized $\tilde{\mathcal{O}}_{i,\rho\sigma}$ matrix elements at each t_f ; (ii) one- and two-loop perturbative scheme conversion of the continuum-extrapolated matrix elements to the $\overline{\text{MS}}$ scheme at $\mu = 2 \text{ GeV}$ for each t_f ; (iii) zero-flow-time, $t_f \rightarrow 0$, extrapolations of the resulting $\overline{\text{MS}}$ -renormalized matrix elements.

At each t_f , the $a \rightarrow 0$ extrapolation is carried out by fitting $\langle H | \tilde{\mathcal{O}}_{i,\rho\sigma} | H \rangle(t_f, a) =$

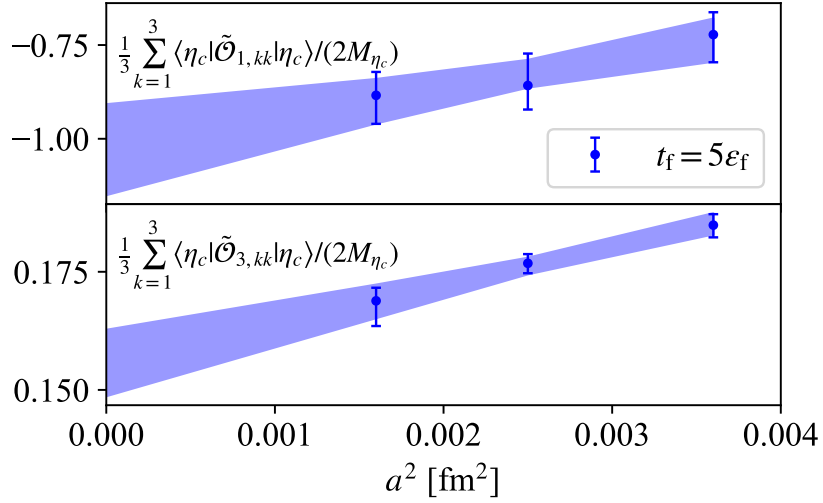


FIG. 1. Continuum extrapolations of hadronic matrix elements of gradient-flow-renormalized EMT components.

$\langle H | \tilde{\mathcal{O}}_{i,\rho\sigma} | H \rangle(t_f, 0) + a^2 X_{i,\rho\sigma}(t_f)$ using uncorrelated bootstrap samples from the three ensembles to determine $\langle H | \tilde{\mathcal{O}}_{i,\rho\sigma} | H \rangle(t_f, 0)$. For all operators and t_f values investigated, the linear a^2 behavior is well supported by the data. Representative examples are shown in Figure 1 for $\sum_{k=1}^3 \langle \eta_c | \tilde{\mathcal{O}}_{1,kk} | \eta_c \rangle / (2M_{\eta_c})$ (upper) and $\sum_{k=1}^3 \langle \eta_c | \tilde{\mathcal{O}}_{3,kk} | \eta_c \rangle / (2M_{\eta_c})$ (lower) at $t_f = 5\epsilon_f$.

The continuum-extrapolated matrix elements are then converted from the gradient-flow scheme to the $\overline{\text{MS}}$ scheme at $\mu = 2$ GeV using $\langle H | \mathcal{O}_i^{\overline{\text{MS}}} | H \rangle(\mu, t_f) = M_{ij}(t_f, \mu) \langle H | \tilde{\mathcal{O}}_j | H \rangle(t_f, 0)$, where $M_{ij}(t_f, \mu)$, with $i, j = 1, \dots, 4$, are the one- and two-loop perturbative matching coefficients [50–52, 58] that incorporate both renormalization and operator mixing. Together with the QCD EoM, this yields $\overline{\text{MS}}$ -renormalized matrix elements of all five operators in Equation 2. To ensure that the scheme conversion remains perturbatively reliable—the $\ln(2t_f\mu^2)$ terms in $M_{ij,\rho\sigma}$ remain small at $\mu = 2$ GeV—we restrict ourselves to a small interval $t_f = 0.00156 \sim 0.00416 \text{ fm}^2$. As shown in Figure 2, within this window the difference between one-loop and two-loop matched results stays small, indicating uncertainty due to higher-order perturbative corrections is under control.

Since Gradient flow smooths the gluon and quark fields over an approximate radius $\sqrt{8t_f}$ [47–49], the small- t_f expansion of the flowed operators receives additional contributions from higher-dimensional operators, leading to residual t_f dependence of the matched matrix elements. To remove these contaminations, we perform a $t_f \rightarrow 0$ extrapolation of the matched matrix elements using $\langle H | \mathcal{O}_{i,\rho\sigma}^{\overline{\text{MS}}} | H \rangle(\mu, t_f) = \langle H | \mathcal{O}_{i,\rho\sigma}^{\overline{\text{MS}}} | H \rangle(\mu) + Y_{i,\rho\sigma} t_f$, with correlated fits to bootstrap samples over the $t_f = 0.00156 \sim 0.00416 \text{ fm}^2$ interval. As illustrated in Figure 2, the data display a clear linear dependence in this range.

V. GRAVITATIONAL FORM FACTORS

From $\langle H | \mathcal{O}_{i,\rho\sigma}^{\overline{\text{MS}}} | H \rangle(\mu)$ we construct $\langle H | T_{X,\rho\sigma}^{\overline{\text{MS}}} | H \rangle(\mu)$ using Equation 3, propagating correlated uncertainties using bootstrap samples.

From here on we present all physical results are in Minkowski space, with Euclidean

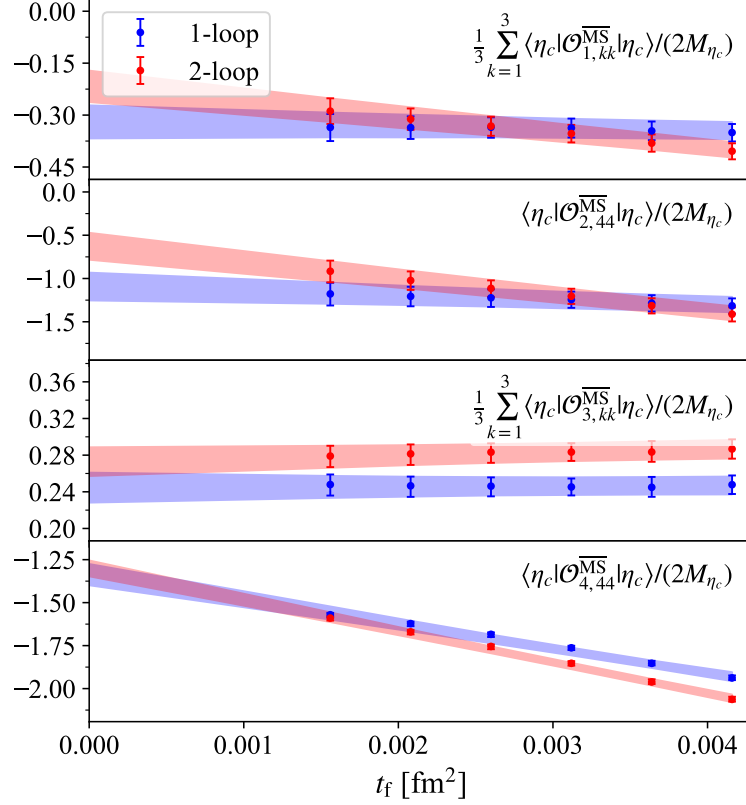


FIG. 2. Flow-time dependence and zero-flow-time extrapolations of hadronic matrix elements of $\overline{\text{MS}}$ -renormalized EMT components at $\mu = 2$ GeV using one-loop (blue) and two-loop (red) perturbative matching.

	η_c		J/ψ		
	$A(0)$	$\bar{C}(0)$	$A(0)$	$\bar{C}(0)$	$\bar{f}(0)$
gluon(g)	0.084(45)	0.058(18)	0.077(35)	-0.146(29)	-0.012(32)
charm(c)	0.918(17)	-0.068(4)	0.926(34)	0.176(87)	0.023(5)
total	1.000(46)	-0.010(18)	0.997(43)	0.030(30)	0.010(32)

TABLE I. Gravitational form factors of η_c (Equation 4) and J/ψ (Equation 5) in the $\overline{\text{MS}}$ scheme and at the scale $\mu = 2$ GeV.

lattice matrix elements converted accordingly.

For the pseudoscalar η_c meson, the rest-frame matrix elements of $\overline{\text{MS}}$ -renormalized EMT components [28, 32],

$$\begin{aligned} \langle \eta_c | T_{X,00}^{\overline{\text{MS}}} | \eta_c \rangle &= 2M_{\eta_c}^2 [A_X(0) + \bar{C}_X(0)], \\ \sum_{k=1}^3 \langle \eta_c | T_{X,kk}^{\overline{\text{MS}}} | \eta_c \rangle &= -6M_{\eta_c}^2 \bar{C}_X(0), \end{aligned} \quad (4)$$

provide two independent relations to extract $\overline{\text{MS}}$ -renormalized GFFs $A_X(0)$ and $\bar{C}_X(0)$ at

vanishing momentum transfer. The $A_X(0)$ gives the partonic momentum fraction and $\bar{C}_X(0)$ encodes the trace contribution.

For the vector J/ψ meson, the rest-frame matrix elements of $\overline{\text{MS}}$ -renormalized EMT components in the state J polarized along the γ_1 direction [32, 82].

$$\begin{aligned}\langle J|T_{X,00}^{\overline{\text{MS}}}|J\rangle &= 2M_{J/\psi}^2[A_X(0) - \frac{1}{2}\bar{C}_X(0) + \frac{1}{4}\bar{f}_X(0)], \\ \langle J|T_{X,11}^{\overline{\text{MS}}}|J\rangle &= 2M_{J/\psi}^2\left[\frac{1}{2}\bar{C}_X(0) + \frac{3}{4}\bar{f}_X(0)\right], \\ \sum_{k=2,3}\langle J|T_{X,kk}^{\overline{\text{MS}}}|J\rangle &= 4M_{J/\psi}^2\left[\frac{1}{2}\bar{C}_X(0) - \frac{1}{4}\bar{f}_X(0)\right],\end{aligned}\quad (5)$$

determine three $\overline{\text{MS}}$ -renormalized GFFs, A_X , \bar{C}_X , and \bar{f}_X , at vanishing momentum transfer.

Table I presents the results of first direct lattice QCD calculations of GFFs \bar{C} and \bar{f} . We obtain $\bar{C}_c(0) + \bar{C}_g(0) = 0$ and, for the vector meson, $\bar{f}_c(0) + \bar{f}_g(0) = 0$ within uncertainties, validating the corresponding trace-anomaly sum rules ¹. We also find, within uncertainties, the longitudinal momentum sum rule for partons $A_c(0) + A_g(0) = 1$ for both η_c and J/ψ .

VI. THE σ TERM USING QCD EOM

The contribution to the hadron mass due to explicit chiral-symmetry breaking for $m_f > 0$ is quantified by

$$\sigma_f = \frac{1}{2M_H}\langle H|\mathcal{O}_{5,00,f}^{\overline{\text{MS}}}|H\rangle = -\frac{1}{4M_H}\langle H|\mathcal{O}_{4,00,f}^{\overline{\text{MS}}}|H\rangle. \quad (6)$$

We utilize the QCD EoM for quark flavor f to eliminate $\mathcal{O}_{5,\rho\sigma,f}^{\overline{\text{MS}}}$ in favor of $\mathcal{O}_{4,\rho\sigma,f}^{\overline{\text{MS}}}$. Since $m_f > 0$ explicitly breaks the scale invariance of classical QCD, the σ term also contributes to the trace of QCD EMT in addition to anomaly generated through quantum corrections.

An example of $\overline{\text{MS}}$ -renormalized σ_c , obtained from $\langle H|\mathcal{O}_{4,00,c}^{\overline{\text{MS}}}|H\rangle$, is shown in [Figure 2](#), where it can be seen that the one- and two-loop matching give consistent results in the $t_f \rightarrow 0$ limit.

VII. HADRON MASS DECOMPOSITIONS

Having determined all necessary $\overline{\text{MS}}$ -renormalized matrix elements we directly validate the sum rules underlying several complementary decompositions of the hadron mass. The Hatta-Rajan-Tanaka (HRT) [7] decomposition based on the rest-frame matrix elements of the trace of $\overline{\text{MS}}$ -renormalized EMT is

$$M_H = \sum_{X=q,g} M_X^{\text{HRT}}, \quad \text{with} \quad M_X^{\text{HRT}} = \frac{\langle H| \left(T_X^{\overline{\text{MS}}}\right)^\rho |H\rangle}{2M_H}. \quad (7)$$

¹ The sign difference of $\bar{C}(0)$ between η_c and J/ψ stems from different Minkowski and polarization-normalization conventions used in the standard Lorentz-covariant parametrization of EMT matrix elements for pseudoscalar [32] and vector [82] mesons.

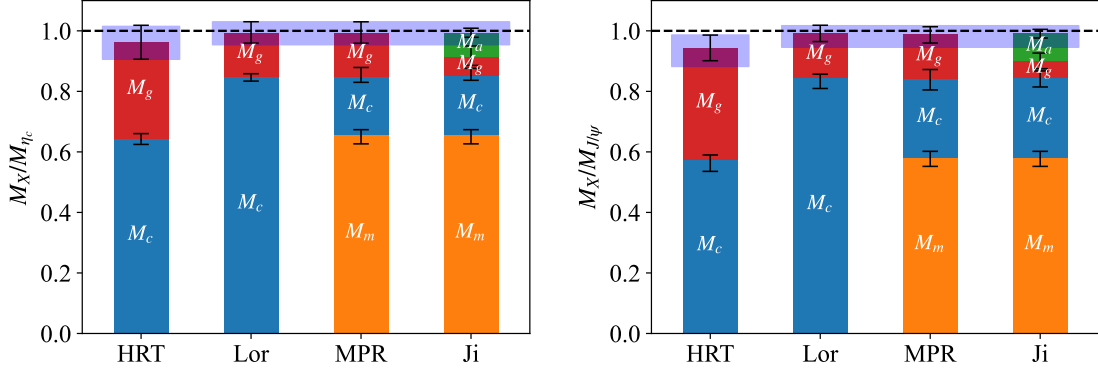


FIG. 3. Hatta-Rajan-Tanaka (HRT, Equation 7), Lorcé (Lor, Equation 8), Metz-Pasquini-Rodini (MPR, Equation 9), and Ji (Ji, Equation 10) decompositions of η_c (left panel) and J/ψ (right panel) masses. All contributions are presented at 2 GeV $\overline{\text{MS}}$ scale using 2-loop gradient-flow to $\overline{\text{MS}}$ matching. The black error bars indicate combined systematic and statistical uncertainty of each individual components. The blue error bands on top indicate combined systematic and statistical uncertainty of the sum over all components in each cases.

The Lorcé [11], Metz-Pasquini-Rodini (MPR) [45, 83], and Ji [9, 10, 57, 84] decompositions are all based on the rest-frame matrix element of $T_{00}^{\overline{\text{MS}}}$, but organize the quark/gluon contributions in different ways. The Lorcé's decomposition in the $\overline{\text{MS}}$ scheme reads

$$M_H = \sum_{X=q,g} M_X^{\text{Lor}}, \quad \text{with} \quad M_X^{\text{Lor}} = \frac{\langle H | T_{X,00}^{\overline{\text{MS}}} | H \rangle}{2M_H}. \quad (8)$$

The MPR decomposition explicitly separates out σ_f , giving

$$\begin{aligned} M_H &= \sum_{X=q,g,m} M_X^{\text{MPR}}, \quad \text{with} \quad M_m^{\text{MPR}} = \sum_f \sigma_f, \\ M_q^{\text{MPR}} &= M_q^{\text{Lor}} - \sum_f \sigma_f, \quad M_g^{\text{MPR}} = M_g^{\text{Lor}}. \end{aligned} \quad (9)$$

The Ji decomposition distinguishes the contributions from the traceless part of the EMT from the trace anomaly part, yielding

$$\begin{aligned} M_H &= \sum_{X=q,g,m,a} M_X^{\text{Ji}}, \quad \text{with} \quad M_m^{\text{Ji}} = M_m^{\text{MPR}}, \\ M_q^{\text{Ji}} &= M_q^{\text{Lor}} - \frac{1}{4} M_q^{\text{HRT}} - \frac{3}{4} M_m^{\text{MPR}}, \\ M_g^{\text{Ji}} &= M_g^{\text{Lor}} - \frac{1}{4} M_g^{\text{HRT}}, \\ M_a^{\text{Ji}} &= \frac{1}{4} [M_q^{\text{HRT}} + M_g^{\text{HRT}} - M_m^{\text{MPR}}]. \end{aligned} \quad (10)$$

Figure 3 presents HRT, Lorcé, MPR, and Ji mass decompositions, all at 2 GeV $\overline{\text{MS}}$ scale, of η_c (left panel) and J/ψ (right panel). For the quark sector we include only the

charm flavor and find all mass rules are satisfied within uncertainty, demonstrating the mutual consistency of these distinct decomposition schemes when evaluated in the same renormalization framework. These show light-quark contributions to charmonia masses are negligible. The dominant contributions to $M_{\eta_c} = 2984.1$ MeV and $M_{J/\psi} = 3096.9$ MeV come from the charm quark: $M_c^{\text{HRT}} = 1918^{+53}_{-54}$ MeV, $M_c^{\text{Lor}} = 2536^{+25}_{-48}$ MeV, and $M_c^{\text{Ji}} + M_m^{\text{Ji}} = 2542^{+26}_{-40}$ MeV for η_c , and $M_c^{\text{HRT}} = 1776^{+51}_{-117}$ MeV, $M_c^{\text{Lor}} = 2617^{+35}_{-110}$ MeV, and $M_c^{\text{Ji}} + M_m^{\text{Ji}} = 2614^{+40}_{-78}$ MeV for J/ψ . Gluons also provide sizable contributions: $M_g^{\text{HRT}} = 953^{+168}_{-167}$ MeV, $M_g^{\text{Lor}} = 426^{+111}_{-100}$ MeV, and $M_g^{\text{Ji}} = 188^{+102}_{-91}$ MeV for η_c , and $M_g^{\text{HRT}} = 1144^{+134}_{-129}$ MeV, $M_g^{\text{Lor}} = 455^{+82}_{-85}$ MeV, and $M_g^{\text{Ji}} = 179^{+78}_{-82}$ MeV for J/ψ . These first-principle QCD calculations demonstrate QCD confinement not only provides substantial gluon-energy contributions but also generates non-negligible trace-anomaly contributions— $M_a^{\text{Ji}} = 231^{+45}_{-44}$ MeV for η_c and $M_a^{\text{Ji}} = 277^{+43}_{-45}$ MeV for J/ψ —to the hadron masses, even for deeply bound $c\bar{c}$ states.

VIII. CONCLUSIONS

In this work, we have presented the first direct lattice-QCD validation of sum rules associated with quark–gluon decomposition of hadron mass. By constructing the QCD energy–momentum tensor nonperturbatively in a gradient-flow scheme, we achieve a formulation that controls operator mixing and avoids power-divergent subtractions, enabling a well-defined continuum limit extrapolation, followed by two-loop matching to the $\overline{\text{MS}}$ scheme and zero-flow-time extrapolations. This establishes a common renormalization framework in which multiple mass decomposition sum rules can be verified simultaneously.

Applying this framework to the η_c and J/ψ charmonia, we demonstrate the consistency of energy-density-based and trace-based decompositions and quantify substantial contributions from gluonic energy and the QCD trace anomaly to heavy quark bound-state masses. The first lattice determination of the gravitational form factor \bar{C} further illustrates the scope of the approach. Beyond charmonium, the methodology developed here provides a general foundation for first-principles studies of hadron mass, spin structure, and gravitational form factors. In particular, it enables access to components of the energy–momentum tensor, such as trace and higher-twist contributions, that are challenging to constrain experimentally, thereby providing essential nonperturbative input complementary to ongoing and future programs at the Thomas Jefferson National Accelerator Facility and the future Electron–Ion Collider.

ACKNOWLEDGMENTS

This material is based upon work supported by the U.S. Department of Energy, Office of Science, Office of Nuclear Physics through Contract No. DE-SC0012704, and within the frameworks of Scientific Discovery through Advanced Computing (SciDAC) award “Fundamental Nuclear Physics at the Exascale and Beyond” and the Topical Collaboration in Nuclear Theory “Heavy-Flavor Theory (HEFTY) for QCD Matter”. This work is supported partly by the National Natural Science Foundation of China under Grants Numbers 12325508, 12293064, and 12293060 as well as the National Key Research and Development Program of China under Contract No. 2022YFA1604900 and the Fundamental Research Funds for the Central Universities, Central China Normal University under Grants No. 30101250314 and No.30106250152.

This research used awards of computer time provided by the Oak Ridge Leadership Computing Facility, which is a DOE Office of Science User Facility supported under Contract DE-AC05-00OR22725; the National Energy Research Scientific Computing Center, a DOE Office of Science User Facility supported by the Office of Science of the U.S. Department of Energy under Contract DE-AC02-05CH11231; and the Nuclear Science Computing Center at Central China Normal University (NSC³).

Work used Grid [85], GPT (Grid Python Toolkit) [86], and rundec [87] software packages.

-
- [1] H. Fritzsch and M. Gell-Mann, Current algebra: Quarks and what else?, eConf **C720906V2**, 135 (1972), [arXiv:hep-ph/0208010](https://arxiv.org/abs/hep-ph/0208010).
- [2] D. J. Gross and F. Wilczek, Ultraviolet Behavior of Nonabelian Gauge Theories, *Phys. Rev. Lett.* **30**, 1343 (1973).
- [3] H. D. Politzer, Reliable Perturbative Results for Strong Interactions?, *Phys. Rev. Lett.* **30**, 1346 (1973).
- [4] J. C. Collins, A. Duncan, and S. D. Joglekar, Trace and Dilatation Anomalies in Gauge Theories, *Phys. Rev. D* **16**, 438 (1977).
- [5] N. K. Nielsen, The Energy Momentum Tensor in a Nonabelian Quark Gluon Theory, *Nucl. Phys. B* **120**, 212 (1977).
- [6] M. A. Shifman, A. I. Vainshtein, and V. I. Zakharov, Remarks on Higgs Boson Interactions with Nucleons, *Phys. Lett. B* **78**, 443 (1978).
- [7] Y. Hatta, A. Rajan, and K. Tanaka, Quark and gluon contributions to the QCD trace anomaly, *JHEP* **12**, 008, [arXiv:1810.05116 \[hep-ph\]](https://arxiv.org/abs/1810.05116).
- [8] X. Ji and Y. Liu, Quantum anomalous energy effects on the nucleon mass, *Sci. China Phys. Mech. Astron.* **64**, 281012 (2021), [arXiv:2101.04483 \[hep-ph\]](https://arxiv.org/abs/2101.04483).
- [9] X.-D. Ji, A QCD analysis of the mass structure of the nucleon, *Phys. Rev. Lett.* **74**, 1071 (1995), [arXiv:hep-ph/9410274](https://arxiv.org/abs/hep-ph/9410274).
- [10] X.-D. Ji, Breakup of hadron masses and energy - momentum tensor of QCD, *Phys. Rev. D* **52**, 271 (1995), [arXiv:hep-ph/9502213](https://arxiv.org/abs/hep-ph/9502213).
- [11] C. Lorcé, On the hadron mass decomposition, *Eur. Phys. J. C* **78**, 120 (2018), [arXiv:1706.05853 \[hep-ph\]](https://arxiv.org/abs/1706.05853).
- [12] C. Lorcé, A. Metz, B. Pasquini, and S. Rodini, Energy-momentum tensor in QCD: nucleon mass decomposition and mechanical equilibrium, *JHEP* **11**, 121, [arXiv:2109.11785 \[hep-ph\]](https://arxiv.org/abs/2109.11785).
- [13] M. V. Polyakov, Generalized parton distributions and strong forces inside nucleons and nuclei, *Phys. Lett. B* **555**, 57 (2003), [arXiv:hep-ph/0210165](https://arxiv.org/abs/hep-ph/0210165).
- [14] C. Lorcé, H. Moutarde, and A. P. Trawiński, Revisiting the mechanical properties of the nucleon, *Eur. Phys. J. C* **79**, 89 (2019), [arXiv:1810.09837 \[hep-ph\]](https://arxiv.org/abs/1810.09837).
- [15] M. V. Polyakov and P. Schweitzer, Forces inside hadrons: pressure, surface tension, mechanical radius, and all that, *Int. J. Mod. Phys. A* **33**, 1830025 (2018), [arXiv:1805.06596 \[hep-ph\]](https://arxiv.org/abs/1805.06596).
- [16] V. D. Burkert, L. Elouadrhiri, and F. X. Girod, The pressure distribution inside the proton, *Nature* **557**, 396 (2018).
- [17] V. D. Burkert, L. Elouadrhiri, F. X. Girod, C. Lorcé, P. Schweitzer, and P. E. Shanahan, Colloquium: Gravitational form factors of the proton, *Rev. Mod. Phys.* **95**, 041002 (2023), [arXiv:2303.08347 \[hep-ph\]](https://arxiv.org/abs/2303.08347).
- [18] A. Accardi *et al.*, Electron Ion Collider: The Next QCD Frontier: Understanding the glue

- that binds us all, *Eur. Phys. J. A* **52**, 268 (2016), arXiv:1212.1701 [nucl-ex].
- [19] R. Abdul Khalek *et al.*, Snowmass 2021 White Paper: Electron Ion Collider for High Energy Physics (2022), arXiv:2203.13199 [hep-ph].
- [20] D. Boer *et al.*, Gluons and the quark sea at high energies: Distributions, polarization, tomography (2011), arXiv:1108.1713 [nucl-th].
- [21] D. Müller, D. Robaschik, B. Geyer, F. M. Dittes, and J. Hořejši, Wave functions, evolution equations and evolution kernels from light ray operators of QCD, *Fortsch. Phys.* **42**, 101 (1994), arXiv:hep-ph/9812448.
- [22] D. Müller, D. Robaschik, B. Geyer, F. M. Dittes, and J. Hořejši, Wave functions, evolution equations and evolution kernels from light ray operators of QCD, *Fortsch. Phys.* **42**, 101 (1994), arXiv:hep-ph/9812448.
- [23] X.-D. Ji, Gauge-Invariant Decomposition of Nucleon Spin, *Phys. Rev. Lett.* **78**, 610 (1997), arXiv:hep-ph/9603249.
- [24] A. V. Radyushkin, Scaling limit of deeply virtual Compton scattering, *Phys. Lett. B* **380**, 417 (1996), arXiv:hep-ph/9604317.
- [25] X.-D. Ji, Deeply virtual Compton scattering, *Phys. Rev. D* **55**, 7114 (1997), arXiv:hep-ph/9609381.
- [26] J. E. Mandula, G. Zweig, and J. Govaerts, Representations of the Rotation Reflection Symmetry Group of the Four-dimensional Cubic Lattice, *Nucl. Phys. B* **228**, 91 (1983).
- [27] M. Gockeler, R. Horsley, E.-M. Ilgenfritz, H. Perlt, P. E. L. Rakow, G. Schierholz, and A. Schiller, Lattice operators for moments of the structure functions and their transformation under the hypercubic group, *Phys. Rev. D* **54**, 5705 (1996), arXiv:hep-lat/9602029.
- [28] D. C. Hackett, P. R. Oare, D. A. Pefkou, and P. E. Shanahan, Gravitational form factors of the pion from lattice QCD, *Phys. Rev. D* **108**, 114504 (2023), arXiv:2307.11707 [hep-lat].
- [29] D. C. Hackett, D. A. Pefkou, and P. E. Shanahan, Gravitational Form Factors of the Proton from Lattice QCD, *Phys. Rev. Lett.* **132**, 251904 (2024), arXiv:2310.08484 [hep-lat].
- [30] D. Brommel, M. Diehl, M. Gockeler, P. Hagler, R. Horsley, D. Pleiter, P. E. L. Rakow, A. Schafer, G. Schierholz, and J. M. Zanotti, Structure of the pion from full lattice QCD, *PoS LAT2005*, 360 (2006), arXiv:hep-lat/0509133.
- [31] P. E. Shanahan and W. Detmold, Gluon gravitational form factors of the nucleon and the pion from lattice QCD, *Phys. Rev. D* **99**, 014511 (2019), arXiv:1810.04626 [hep-lat].
- [32] D. A. Pefkou, D. C. Hackett, and P. E. Shanahan, Gluon gravitational structure of hadrons of different spin, *Phys. Rev. D* **105**, 054509 (2022), arXiv:2107.10368 [hep-lat].
- [33] M. Löffler, P. Wein, T. Wurm, S. Weishäupl, D. Jenkins, R. Rödl, A. Schäfer, and L. Walter (RQCD), Mellin moments of spin dependent and independent PDFs of the pion and rho meson, *Phys. Rev. D* **105**, 014505 (2022), arXiv:2108.07544 [hep-lat].
- [34] C. Alexandrou *et al.*, Moments of nucleon generalized parton distributions from lattice QCD simulations at physical pion mass, *Phys. Rev. D* **101**, 034519 (2020), arXiv:1908.10706 [hep-lat].
- [35] G. S. Bali, S. Collins, M. Göckeler, R. Rödl, A. Schäfer, and A. Sternbeck, Nucleon generalized form factors from two-flavor lattice QCD, *Phys. Rev. D* **100**, 014507 (2019), arXiv:1812.08256 [hep-lat].
- [36] S. Bhattacharya, K. Cichy, M. Constantinou, X. Gao, A. Metz, J. Miller, S. Mukherjee, P. Petreczky, F. Steffens, and Y. Zhao, Moments of axial-vector GPD from lattice QCD: quark helicity, orbital angular momentum, and spin-orbit correlation, *JHEP* **01**, 146, arXiv:2410.03539 [hep-lat].

- [37] S. Bhattacharya, K. Cichy, M. Constantinou, X. Gao, A. Metz, J. Miller, S. Mukherjee, P. Petreczky, F. Steffens, and Y. Zhao, Moments of proton GPDs from the OPE of nonlocal quark bilinears up to NNLO, *Phys. Rev. D* **108**, 014507 (2023), [arXiv:2305.11117 \[hep-lat\]](#).
- [38] H. Dutrieux, R. G. Edwards, C. Egerer, J. Karpie, C. Monahan, K. Orginos, A. Radyushkin, D. Richards, E. Romero, and S. Zafeiropoulos (HadStruc), Towards unpolarized GPDs from pseudo-distributions, *JHEP* **08**, 162, [arXiv:2405.10304 \[hep-lat\]](#).
- [39] B. Wang, F. He, G. Wang, T. Draper, J. Liang, K.-F. Liu, and Y.-B. Yang (χ QCD), Trace anomaly form factors from lattice QCD, *Phys. Rev. D* **109**, 094504 (2024), [arXiv:2401.05496 \[hep-lat\]](#).
- [40] W. Sun, Y. Chen, P. Sun, and Y.-B. Yang (χ QCD), Gluons in charmoniumlike states, *Phys. Rev. D* **103**, 094503 (2021), [arXiv:2012.06228 \[hep-lat\]](#).
- [41] Y.-B. Yang, Y. Chen, T. Draper, M. Gong, K.-F. Liu, Z. Liu, and J.-P. Ma, Meson Mass Decomposition from Lattice QCD, *Phys. Rev. D* **91**, 074516 (2015), [arXiv:1405.4440 \[hep-ph\]](#).
- [42] Y.-B. Yang, J. Liang, Y.-J. Bi, Y. Chen, T. Draper, K.-F. Liu, and Z. Liu, Proton Mass Decomposition from the QCD Energy Momentum Tensor, *Phys. Rev. Lett.* **121**, 212001 (2018), [arXiv:1808.08677 \[hep-lat\]](#).
- [43] F. He, P. Sun, and Y.-B. Yang (χ QCD), Demonstration of the hadron mass origin from the QCD trace anomaly, *Phys. Rev. D* **104**, 074507 (2021), [arXiv:2101.04942 \[hep-lat\]](#).
- [44] B. Hu, H. Du, X. Jiang, K.-F. Liu, P. Sun, and Y.-B. Yang, Unveiling the Strong Interaction origin of Baryon Masses with Lattice QCD (2024), [arXiv:2411.18402 \[hep-lat\]](#).
- [45] A. Metz, B. Pasquini, and S. Rodini, Revisiting the proton mass decomposition, *Phys. Rev. D* **102**, 114042 (2020), [arXiv:2006.11171 \[hep-ph\]](#).
- [46] R. Narayanan and H. Neuberger, Infinite N phase transitions in continuum Wilson loop operators, *JHEP* **03**, 064, [arXiv:hep-th/0601210](#).
- [47] M. Lüscher, Trivializing maps, the Wilson flow and the HMC algorithm, *Commun. Math. Phys.* **293**, 899 (2010), [arXiv:0907.5491 \[hep-lat\]](#).
- [48] M. Lüscher, Properties and uses of the Wilson flow in lattice QCD, *JHEP* **08**, 071, [Erratum: *JHEP* 03, 092 (2014)], [arXiv:1006.4518 \[hep-lat\]](#).
- [49] M. Lüscher and P. Weisz, Perturbative analysis of the gradient flow in non-abelian gauge theories, *JHEP* **02**, 051, [arXiv:1101.0963 \[hep-th\]](#).
- [50] H. Suzuki, Energy-momentum tensor from the Yang–Mills gradient flow, *PTEP* **2013**, 083B03 (2013), [Erratum: *PTEP* 2015, 079201 (2015)], [arXiv:1304.0533 \[hep-lat\]](#).
- [51] H. Makino and H. Suzuki, Lattice energy-momentum tensor from the Yang–Mills gradient flow—incusion of fermion fields, *PTEP* **2014**, 063B02 (2014), [Erratum: *PTEP* 2015, 079202 (2015)], [arXiv:1403.4772 \[hep-lat\]](#).
- [52] Y. Taniguchi, S. Ejiri, R. Iwami, K. Kanaya, M. Kitazawa, H. Suzuki, T. Umeda, and N. Wakabayashi (WHOT-QCD), Exploring $N_f = 2+1$ QCD thermodynamics from the gradient flow, *Phys. Rev. D* **96**, 014509 (2017), [Erratum: *Phys. Rev. D* 99, 059904 (2019)], [arXiv:1609.01417 \[hep-lat\]](#).
- [53] Y. Taniguchi, S. Ejiri, K. Kanaya, M. Kitazawa, A. Suzuki, H. Suzuki, and T. Umeda (WHOT-QCD), Energy-momentum tensor correlation function in $N_f = 2 + 1$ full QCD at finite temperature, *EPJ Web Conf.* **175**, 07013 (2018), [arXiv:1711.02262 \[hep-lat\]](#).
- [54] F. J. Belinfante, Consequences of the Postulate of a Complete Commuting Set of Observables in Quantum Electrodynamics, *Phys. Rev.* **128**, 2832 (1962).
- [55] A. V. Belitsky and A. V. Radyushkin, Unraveling hadron structure with generalized parton

- distributions, *Phys. Rept.* **418**, 1 (2005), arXiv:hep-ph/0504030.
- [56] A. Freese, Noether's theorems and the energy-momentum tensor in quantum gauge theories, *Phys. Rev. D* **106**, 125012 (2022), arXiv:2112.00047 [hep-th].
- [57] X. Ji, Y. Liu, and A. Schäfer, Scale symmetry breaking, quantum anomalous energy and proton mass decomposition, *Nucl. Phys. B* **971**, 115537 (2021), arXiv:2105.03974 [hep-ph].
- [58] R. V. Harlander, Y. Kluth, and F. Lange, The two-loop energy-momentum tensor within the gradient-flow formalism, *Eur. Phys. J. C* **78**, 944 (2018), [Erratum: Eur.Phys.J.C 79, 858 (2019)], arXiv:1808.09837 [hep-lat].
- [59] E. Follana, Q. Mason, C. Davies, K. Hornbostel, G. P. Lepage, J. Shigemitsu, H. Trottier, and K. Wong (HPQCD, UKQCD), Highly improved staggered quarks on the lattice, with applications to charm physics, *Phys. Rev. D* **75**, 054502 (2007), arXiv:hep-lat/0610092.
- [60] A. Bazavov *et al.* (HotQCD), Equation of state in (2+1)-flavor QCD, *Phys. Rev. D* **90**, 094503 (2014), arXiv:1407.6387 [hep-lat].
- [61] A. Bazavov *et al.*, Meson screening masses in (2+1)-flavor QCD, *Phys. Rev. D* **100**, 094510 (2019), arXiv:1908.09552 [hep-lat].
- [62] T. Izubuchi, L. Jin, C. Kallidonis, N. Karthik, S. Mukherjee, P. Petreczky, C. Shugert, and S. Syritsyn, Valence parton distribution function of pion from fine lattice, *Phys. Rev. D* **100**, 034516 (2019), arXiv:1905.06349 [hep-lat].
- [63] X. Gao, L. Jin, C. Kallidonis, N. Karthik, S. Mukherjee, P. Petreczky, C. Shugert, S. Syritsyn, and Y. Zhao, Valence parton distribution of the pion from lattice QCD: Approaching the continuum limit, *Phys. Rev. D* **102**, 094513 (2020), arXiv:2007.06590 [hep-lat].
- [64] X. Gao, N. Karthik, S. Mukherjee, P. Petreczky, S. Syritsyn, and Y. Zhao, Towards studying the structural differences between the pion and its radial excitation, *Phys. Rev. D* **103**, 094510 (2021), arXiv:2101.11632 [hep-lat].
- [65] X. Gao, N. Karthik, S. Mukherjee, P. Petreczky, S. Syritsyn, and Y. Zhao, Pion form factor and charge radius from lattice QCD at the physical point, *Phys. Rev. D* **104**, 114515 (2021), arXiv:2102.06047 [hep-lat].
- [66] X. Gao, A. D. Hanlon, S. Mukherjee, P. Petreczky, P. Scior, S. Syritsyn, and Y. Zhao, Lattice QCD Determination of the Bjorken-x Dependence of Parton Distribution Functions at Next-to-Next-to-Leading Order, *Phys. Rev. Lett.* **128**, 142003 (2022), arXiv:2112.02208 [hep-lat].
- [67] X. Gao, A. D. Hanlon, N. Karthik, S. Mukherjee, P. Petreczky, P. Scior, S. Syritsyn, and Y. Zhao, Pion distribution amplitude at the physical point using the leading-twist expansion of the quasi-distribution-amplitude matrix element, *Phys. Rev. D* **106**, 074505 (2022), arXiv:2206.04084 [hep-lat].
- [68] X. Gao, A. D. Hanlon, N. Karthik, S. Mukherjee, P. Petreczky, P. Scior, S. Shi, S. Syritsyn, Y. Zhao, and K. Zhou, Continuum-extrapolated NNLO valence PDF of the pion at the physical point, *Phys. Rev. D* **106**, 114510 (2022), arXiv:2208.02297 [hep-lat].
- [69] X. Gao, A. D. Hanlon, J. Holligan, N. Karthik, S. Mukherjee, P. Petreczky, S. Syritsyn, and Y. Zhao, Unpolarized proton PDF at NNLO from lattice QCD with physical quark masses, *Phys. Rev. D* **107**, 074509 (2023), arXiv:2212.12569 [hep-lat].
- [70] X. Gao, W.-Y. Liu, and Y. Zhao, Parton distributions from boosted fields in the Coulomb gauge, *Phys. Rev. D* **109**, 094506 (2024), arXiv:2306.14960 [hep-ph].
- [71] X. Gao, A. D. Hanlon, S. Mukherjee, P. Petreczky, Q. Shi, S. Syritsyn, and Y. Zhao, Transversity PDFs of the proton from lattice QCD with physical quark masses, *Phys. Rev. D* **109**, 054506 (2024), arXiv:2310.19047 [hep-lat].
- [72] H.-T. Ding, X. Gao, A. D. Hanlon, S. Mukherjee, P. Petreczky, Q. Shi, S. Syritsyn, R. Zhang,

- and Y. Zhao, QCD Predictions for Meson Electromagnetic Form Factors at High Momenta: Testing Factorization in Exclusive Processes, *Phys. Rev. Lett.* **133**, 181902 (2024), [arXiv:2404.04412 \[hep-lat\]](https://arxiv.org/abs/2404.04412).
- [73] I. Cloet, X. Gao, S. Mukherjee, S. Syritsyn, N. Karthik, P. Petreczky, R. Zhang, and Y. Zhao, Lattice QCD calculation of x-dependent meson distribution amplitudes at physical pion mass with threshold logarithm resummation, *Phys. Rev. D* **110**, 114502 (2024), [arXiv:2407.00206 \[hep-lat\]](https://arxiv.org/abs/2407.00206).
- [74] H.-T. Ding, X. Gao, S. Mukherjee, P. Petreczky, Q. Shi, S. Syritsyn, and Y. Zhao, Three-dimensional imaging of pion using lattice QCD: generalized parton distributions, *JHEP* **02**, 056, [arXiv:2407.03516 \[hep-lat\]](https://arxiv.org/abs/2407.03516).
- [75] X. Gao, J. He, R. Zhang, and Y. Zhao, Systematic Uncertainties from Gribov Copies in Lattice Calculation of Parton Distributions in the Coulomb Gauge, *Chin. Phys. Lett.* **41**, 121201 (2024), [arXiv:2408.05910 \[hep-lat\]](https://arxiv.org/abs/2408.05910).
- [76] D. Bollweg, X. Gao, J. He, S. Mukherjee, and Y. Zhao, Transverse-momentum-dependent pion structures from lattice QCD: Collins-Soper kernel, soft factor, TMDWF, and TMDPDF, *Phys. Rev. D* **112**, 034501 (2025), [arXiv:2504.04625 \[hep-lat\]](https://arxiv.org/abs/2504.04625).
- [77] X. Gao, S. Mukherjee, Q. Shi, F. Yao, and Y. Zhao, Skewness-dependent Moments of Pion GPD from Nonlocal Quark-Bilinear Correlators (2025), [arXiv:2511.01818 \[hep-lat\]](https://arxiv.org/abs/2511.01818).
- [78] A. Hasenfratz and F. Knechtli, Flavor symmetry and the static potential with hypercubic blocking, *Phys. Rev. D* **64**, 034504 (2001), [arXiv:hep-lat/0103029](https://arxiv.org/abs/hep-lat/0103029).
- [79] A. Ramos and S. Sint, Symanzik improvement of the gradient flow in lattice gauge theories, *Eur. Phys. J. C* **76**, 15 (2016), [arXiv:1508.05552 \[hep-lat\]](https://arxiv.org/abs/1508.05552).
- [80] M. Luscher, Chiral symmetry and the Yang–Mills gradient flow, *JHEP* **04**, 123, [arXiv:1302.5246 \[hep-lat\]](https://arxiv.org/abs/1302.5246).
- [81] E. Shintani, R. Arthur, T. Blum, T. Izubuchi, C. Jung, and C. Lehner, Covariant approximation averaging, *Phys. Rev. D* **91**, 114511 (2015), [arXiv:1402.0244 \[hep-lat\]](https://arxiv.org/abs/1402.0244).
- [82] M. V. Polyakov and B.-D. Sun, Gravitational form factors of a spin one particle, *Phys. Rev. D* **100**, 036003 (2019), [arXiv:1903.02738 \[hep-ph\]](https://arxiv.org/abs/1903.02738).
- [83] S. Rodini, A. Metz, and B. Pasquini, Mass sum rules of the electron in quantum electrodynamics, *JHEP* **09**, 067, [arXiv:2004.03704 \[hep-ph\]](https://arxiv.org/abs/2004.03704).
- [84] X. Ji, Proton mass decomposition: naturalness and interpretations, *Front. Phys. (Beijing)* **16**, 64601 (2021), [arXiv:2102.07830 \[hep-ph\]](https://arxiv.org/abs/2102.07830).
- [85] P. Boyle, A. Yamaguchi, G. Cossu, and A. Portelli, Grid: A next generation data parallel c++ qcd library (2015), [arXiv:1512.03487 \[hep-lat\]](https://arxiv.org/abs/1512.03487).
- [86] C. Lehner *et al.*, Grid python toolkit (gpt), <https://github.com/lehner/gpt>.
- [87] K. G. Chetyrkin, J. H. Kuhn, and M. Steinhauser, RunDec: A Mathematica package for running and decoupling of the strong coupling and quark masses, *Comput. Phys. Commun.* **133**, 43 (2000), [arXiv:hep-ph/0004189](https://arxiv.org/abs/hep-ph/0004189).
- [88] S. Navas *et al.* (Particle Data Group), Review of particle physics, *Phys. Rev. D* **110**, 030001 (2024).

Appendix A: Renormalized EMT Operators via Gradient Flow

To compute EMT matrix elements on the lattice, one must address operator renormalization. Gluonic operators, in particular, suffer from power divergences and complicated

operator mixing. The gradient flow method provides a systematic solution [46–49]: by evolving fields along a fictitious flow time t_f , short-distance fluctuations are suppressed, rendering flowed operators finite at nonzero t_f without requiring further renormalization, and enabling a well-defined continuum limit by taking $a \rightarrow 0$ at fixed physical t_f .

For the gauge field $B_\mu(t_f, x)$, the flow equation is:

$$\partial_{t_f} B_\mu(t_f, x) = D_\nu F_{\nu\mu}(t_f, x), \quad B_\mu(0, x) = A_\mu(x), \quad (\text{A1})$$

and for the fermion field $\chi(t_f, x)$,

$$\partial_{t_f} \chi(t_f, x) = \Delta \chi(t_f, x), \quad \chi(0, x) = \psi(x). \quad (\text{A2})$$

where D_ν is the gauge-covariant derivative and Δ is the covariant Laplacian. The flowed fields are smooth and free from power-divergent mixing at nonzero t_f , making them suitable for defining composite operators without further renormalization.

We construct the flowed versions of the relevant EMT operators using the flowed gauge and fermion fields, subtracting their vacuum expectation values (VEV) to eliminate contributions from the vacuum.

For the gluonic sector, the flowed operators are given by,

$$\begin{aligned} \tilde{\mathcal{O}}_{1,\rho\sigma}(t_f, x) &\equiv 2\text{Tr}^c [F_{\rho\omega}(t_f, x)F_{\sigma\omega}(t_f, x)], \\ \tilde{\mathcal{O}}_{2,\rho\sigma}(t_f, x) &\equiv 2\delta_{\rho\sigma}\text{Tr}^c [F_{\rho\sigma}(t_f, x)F_{\rho\sigma}(t_f, x)], \end{aligned} \quad (\text{A3})$$

where the field strength tensor is constructed from the clover definition of the flowed link fields.

For the quark sector, we use ringed fermion fields $\mathring{\chi}$ and $\mathring{\bar{\chi}}$ [51], which cancel the wavefunction renormalization by construction:

$$\begin{aligned} \mathring{\chi}_f(t_f, x) &\equiv \sqrt{\frac{-6}{(4\pi t_f)^2 \langle \mathring{\bar{\chi}}_f(t_f, x) \mathring{\not{D}} \chi_f(t_f, x) \rangle}} \chi_f(t_f, x), \\ \mathring{\bar{\chi}}_f(t_f, x) &\equiv \sqrt{\frac{-6}{(4\pi t_f)^2 \langle \mathring{\bar{\chi}}_f(t_f, x) \mathring{\not{D}} \chi_f(t_f, x) \rangle}} \bar{\chi}_f(t_f, x). \end{aligned} \quad (\text{A4})$$

Using these, we define the flowed fermionic operators as,

$$\begin{aligned} \tilde{\mathcal{O}}_{3,\rho\sigma}(t_f, x) &\equiv \sum_f \mathring{\bar{\chi}}_f(t_f, x) \left(\gamma_\mu \overset{\leftrightarrow}{D}_\nu + \gamma_\nu \overset{\leftrightarrow}{D}_\mu \right) \mathring{\chi}_f(t_f, x), \\ \tilde{\mathcal{O}}_{4,\rho\sigma}(t_f, x) &\equiv \delta_{\rho\sigma} \sum_f \mathring{\bar{\chi}}_f(t_f, x) \overset{\leftrightarrow}{\mathring{\not{D}}} \mathring{\chi}_f(t_f, x). \end{aligned} \quad (\text{A5})$$

These flowed operators are finite and related to the renormalized EMT in the $\overline{\text{MS}}$ scheme through a small-flow-time matching procedure $\langle H | \mathcal{O}_i^{\overline{\text{MS}}} | H \rangle(\mu, t_f) = M_{ij}(t_f, \mu) \langle H | \tilde{\mathcal{O}}_j | H \rangle(t_f, 0)$ with $i, j = 1, 2, 3, 4$, as described in the main text [50–52, 58]. The relation is valid up to $O(t_f)$ corrections, which are later removed by an extrapolation to $t_f \rightarrow 0$.

a [fm]	N_s	N_t	$m_s^{\text{sea}}/m_l^{\text{sea}}$	M_π^{sea} [MeV]	c_{sw}	am_c^{val}
0.06	48	64	20	160	1.0336	0.306
0.05	64				1.030934	0.236
0.04	64				1.02868	0.167

TABLE II. Summary of gauge ensemble parameters.

inserted	a [fm]	N_{conf}	N_{src} sloppy	N_{src} exact	σ_{sm}/a	N_{sm}
$\tilde{\mathcal{O}}_1, \tilde{\mathcal{O}}_2$	0.06	556	512	16	0	0
	0.05	580			3	30
	0.04	599			4	40
$\tilde{\mathcal{O}}_3, \tilde{\mathcal{O}}_4$	0.06	50	0	10	4	40
	0.05	50			4.8	48
	0.04	50			6	60

TABLE III. The measurement details are summarized, including the number of configurations (N_{conf}), number of sources per configuration (N_{src}), Gaussian smearing parameters—smearing width σ_{sm} and number of steps N_{sm} . For N_{src} , “sloppy” sources refer to single-precision with a tolerance 10^{-8} , while “exact” sources use double precision with a tolerance 10^{-18} .

Appendix B: Details of lattice setup

This section provides details on the construction of two-point and three-point correlation functions, the application of gradient flow, and the computation of flowed operator matrix elements in our study.

We compute both connected and disconnected three-point (3pt) functions involving flowed quark and gluon EMT operators as defined in [Equation A3](#) and [Equation A5](#). For the gluon sector, which enters entirely through disconnected diagrams, we employ the all-mode averaging (AMA) technique [\[81\]](#) to improve statistical precision. Each configuration includes 512 “sloppy” sources computed in single precision with residual tolerance 10^{-8} , and 16 “exact” sources computed in double precision with tolerance 10^{-18} . The number of configurations and measurement details are summarized in Table [III](#).

In the quark sector, we evaluate only connected three-point functions, which are expected to dominate for charm quarks. The corresponding three-point correlators are constructed in the standard way using the sequential-source technique for connected insertions. For each ensemble, we analyze 50 gauge configurations with 10 exact source positions per configuration. We explicitly verify that charm-quark disconnected contributions are negligible compared with both the connected charm and the gluon contributions, as shown in [Figure 15](#) and discussed later. We therefore omit contributions from light and strange quarks. Our final results demonstrate that the retained connected charm and disconnected gluon contributions are sufficient to reproduce the charmonium mass spectrum within uncertainties.

To enhance the overlap with the charmonium ground states, we apply Gaussian smearing to both the source and sink quark fields on the finer lattices. This is implemented via gauge-covariant Wuppertal smearing, which approximates a Gaussian profile through repeated

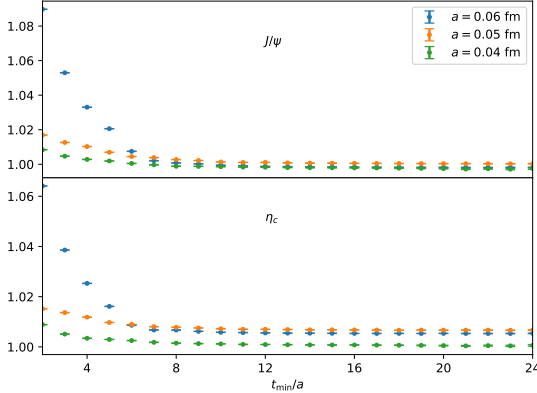


FIG. 4. E_0/E_0^{PDG} [88] of η_c and J/ψ determined from 2-state fit of the 2pt functions are shown for three gauge ensembles, as a function of t_{\min} . The fit range is $[t_{\min}, 32a]$.

applications of the spatial covariant Laplacian:

$$\begin{aligned} \psi(x) &\rightarrow \left(1 + \frac{\sigma_{\text{sm}}^2}{4N_{\text{sm}}} \Delta\right)^{N_{\text{sm}}} \psi(x), \\ \Delta\psi(x) &\equiv \sum_{\mu=1}^3 [U_\mu(x)\psi(x + \hat{\mu}) + U_\mu^\dagger(x - \hat{\mu})\psi(x - \hat{\mu}) - 2\psi(x)], \end{aligned} \quad (\text{B1})$$

where Δ denotes the spatial gauge-covariant Laplacian. The smearing parameters ($\sigma_{\text{sm}}, N_{\text{sm}}$) used for the smeared ensembles are listed in Table III. To further suppress excited-state contamination, we perform the three-point function measurements with large source-sink separations, $t \in [22a, 32a]$.

We apply gradient flow to systematically renormalize the quark and gluon fields in a non-perturbative manner, as discussed in main text. Specifically, gluon operators are constructed from the flowed gauge fields at finite flow time t_f , while quark operators are built from the flowed valence propagators using fermion flow techniques [80]. To obtain the correct EMT in the continuum limit, it is necessary to extrapolate $t_f \rightarrow 0$. Therefore, we perform measurements at multiple values of t_f (in physical units) for all three ensembles. Measurements are performed in units of $\epsilon_f = 5.1984 \times 10^{-4}$, fm 2 , while the fields are evolved using integration step sizes between $\epsilon_f/40$ and $\epsilon_f/2$.

For operators involving ringed fermion fields, we compute the necessary vacuum expectation values including $\langle \bar{\chi}_f(t_f, x) \overset{\leftrightarrow}{D} \chi_f(t_f, x) \rangle$, as described in Equation A4. This requires estimating all-to-all propagators. To this end, we employ Z_2 noise vectors with 10 random sources per configuration. Our tests confirm that for charm quarks, this setup ensures systematic uncertainty below 10^{-4} , which is subdominant relative to our typical statistical uncertainties of 10^{-3} or larger.

Appendix C: Two-point functions and charmonium mass

Extracting hadronic matrix elements of the EMT requires knowledge of the ground-state contribution to the relevant three-point functions. To isolate the ground-state signal, we

analyze meson two-point (2pt) correlation functions, which provide access to the spectrum and amplitudes of low-lying states. The Euclidean two-point function is defined as:

$$C_{\Gamma}^{2\text{pt}}(t) \equiv \sum_{\mathbf{x}} \langle \bar{c}(x) \Gamma c(x) \bar{c}(x_0) \Gamma c(x_0) \rangle = - \sum_{\mathbf{x}} \text{Tr} [S_c(x_0|x) \Gamma S_c(x|x_0) \Gamma], \quad (\text{C1})$$

where $S_c(x|x_0)$ denotes the charm quark propagator from source $x_0 \equiv (\mathbf{x}_0, 0)$ to sink $x \equiv (\mathbf{x}, t)$, and the trace is taken over spin and color indices. The gamma matrix Γ specifies the meson interpolator: $\Gamma = \gamma_5$ corresponds to the pseudoscalar η_c channel, while $\Gamma = \gamma_{\lambda}$ corresponds to the vector J/ψ channel with polarization along the λ -th spatial direction. We average over the $\lambda = 1, 2, 3$ for J/ψ to reduce statistical noise and improve rotational symmetry. The spatial sum over \mathbf{x} projects onto zero-momentum states. In this study, we neglect the quark-line disconnected contributions to the charmonium 2pt functions.

To quantitatively isolate the ground-state and subtract excited-state contamination, we perform correlated two-state fits to the 2pt functions using the ansatz,

$$C^{2\text{pt}}(t) = \sum_{n=0}^{n_{\text{max}}} |Z_n|^2 [e^{-E_n t} + e^{-E_n (N_t a - t)}], \quad (\text{C2})$$

where E_n and Z_n are the energy and overlap amplitude of the n -th state, and N_t is the temporal extent of the lattice. We set $n_{\text{max}} = 1$ to account for the leading excited state.

Figure 4 shows the ratio between our fitted ground-state energies and the corresponding physical meson masses reported by the Particle Data Group (PDG) [88], i.e., E_0/E_0^{PDG} , for the η_c (lower panel) and J/ψ (upper panel). These results are obtained from two-state fits to the 2pt correlators on all three ensembles, using fit ranges $[t_{\text{min}}, 32a]$ with varying t_{min} . The ratios are remarkably close to unity, with deviations below 1%, indicating that our bare charm-quark mass is accurately tuned to reproduce the physical charmonium spectrum.

The fitted values of E_0 and E_1 from each bootstrap sample are used in the subsequent analysis of three-point functions to isolate ground-state matrix elements of the energy-momentum tensor.

Appendix D: Three-point functions of flowed quark EMT operators

The matrix elements of the EMT are extracted from three-point (3pt) correlation functions, where the EMT operator is inserted between interpolating operators for charmonium states. Only the operators $\tilde{\mathcal{O}}_{3,\rho\sigma}$ and $\tilde{\mathcal{O}}_{4,\rho\sigma}$ as defined in Equation A5 are required to reconstruct the physical matrix elements of the quark EMT. Since $\tilde{\mathcal{O}}_{4,\rho\sigma}$ is the trace of $\tilde{\mathcal{O}}_{3,\rho\sigma}$, it suffices to extract only the matrix elements of $\tilde{\mathcal{O}}_{3,\rho\sigma}$. The 3pt function is defined as,

$$C_{q,\Gamma}^{\rho\sigma}(t, \tau) \equiv \sum_{\mathbf{x}} \langle \bar{c}(x) \Gamma c(x) \tilde{\mathcal{O}}_{3,\rho\sigma}(\tau) \bar{c}(x_0) \Gamma c(x_0) \rangle, \quad (\text{D1})$$

where the operator insertion is defined by,

$$\tilde{\mathcal{O}}_{3,\rho\sigma}(\tau) = \sum_{\mathbf{y}} \tilde{\mathcal{O}}_{3,\rho\sigma}(y). \quad (\text{D2})$$

Here, $x_0 \equiv (\mathbf{x}_0, 0)$, $y \equiv (\mathbf{y}, \tau)$, and $x \equiv (\mathbf{x}, t)$ denote the coordinates of the source, operator inserted, and sink, respectively. The temporal variables t and τ correspond to the source-sink separation and the operator insertion time. The gamma matrix Γ correspond to the

meson interpolators, with choices depending on the meson channel, as discussed previously. The corresponding three-point correlators are constructed in the standard way using the sequential-source technique for connected insertions.

The covariant derivative $\overset{\leftrightarrow}{D}_\mu$ in the EMT operator is discretized on the lattice in a symmetric form:

$$\begin{aligned}\overset{\leftrightarrow}{D} &\equiv \vec{D} - \overset{\leftarrow}{D}, \\ \vec{D}_\mu c(y) &\equiv \frac{1}{2} [U_\mu(y)c(y + \hat{\mu}) - U_\mu(y - \hat{\mu})^\dagger c(y - \hat{\mu})], \\ \bar{c}(y)\overset{\leftarrow}{D}_\mu &\equiv \frac{1}{2} [\bar{c}(y + \hat{\mu})U_\mu(y)^\dagger - \bar{c}(y - \hat{\mu})U_\mu(y - \hat{\mu})].\end{aligned}\quad (\text{D3})$$

To achieve nonperturbative renormalization and eliminate short-distance singularities, we construct the EMT operator using flowed fields. Specifically, we replace the local operator $\bar{c}(y)\overset{\leftrightarrow}{D}_\mu c(y)$ by its flowed counterpart:

$$\bar{c}(t_f, y)\overset{\leftrightarrow}{D}_\nu(t_f)c(t_f, y), \quad (\text{D4})$$

where both the quark fields and the gauge links entering the derivative operator are defined at positive flow time t_f .

The flowed fermion fields are defined by the fermion flow equations [80]. In practice, we implement the fermion flow at the level of Wick contractions by convolving the unflowed charm-quark propagators with the fermion flow kernel,

$$\begin{aligned}\langle \bar{c}(t_f, y) c(x) \rangle &= \sum_z K(t_f, y; 0, z) S_c(z|x), \\ \langle c(x) \bar{c}(t_f, y) \rangle &= \sum_z S_c(x|z) K^\dagger(t_f, y; 0, z),\end{aligned}\quad (\text{D5})$$

where S_c is the unflowed charm-quark propagator and $K(t_f, y; 0, z)$ is the fermion flow kernel. The kernel is proportional to the identity in Dirac space and acts as a gauge-covariant smearing function in color and position space. In the $t_f \rightarrow 0$ limit it reduces to a delta function,

$$\lim_{t_f \rightarrow 0} K(t_f, y; 0, z) = \delta_{yz}. \quad (\text{D6})$$

These relations allow us to construct flowed three-point functions entirely from the unflowed propagators together with the known flow kernel, so that no additional flowed inversions are required.

Appendix E: Three-point functions of flowed gluon EMT operators

The matrix elements of the gluon EMT are extracted from three-point correlation functions with gluonic operator insertions. Unlike the quark case, where connected diagrams dominate, the gluon EMT contributes only through disconnected diagrams. The gluon EMT is constructed from two operators, $\tilde{\mathcal{O}}_{1,\rho\sigma}$ and $\tilde{\mathcal{O}}_{2,\rho\sigma}$, as defined in [Equation A3](#). As noted earlier, $\tilde{\mathcal{O}}_{2,\rho\sigma}$ is proportional to the trace of $\tilde{\mathcal{O}}_{1,\rho\sigma}$, so we only need to evaluate matrix elements of $\tilde{\mathcal{O}}_{1,\rho\sigma}$ to reconstruct the full gluon EMT.

The gluonic three-point correlation function is defined as,

$$C_{g,\Gamma}^{\rho\sigma}(t,\tau) = \sum_{\mathbf{x},\mathbf{y}} \langle \mathcal{O}_\Gamma(\mathbf{x},t) \tilde{\mathcal{O}}_{1,\rho\sigma}(\mathbf{y},\tau) \mathcal{O}_\Gamma^\dagger(\mathbf{0},0) \rangle - \langle C_\Gamma^{2\text{pt}}(t) \rangle \sum_{\mathbf{y}} \langle \tilde{\mathcal{O}}_{1,\rho\sigma}(\mathbf{y},\tau) \rangle, \quad (\text{E1})$$

where $C_\Gamma^{2\text{pt}}$ is defined in [Equation C1](#), and the operator insertion is summed over spatial positions at time slice τ . The subtraction removes vacuum contributions.

The gluon field strength tensor $F_{\rho\sigma}(x)$ is constructed using a clover-type discretization:

$$\begin{aligned} U_{\rho\sigma}(x) &= U_\rho(x)U_\sigma(x + \hat{\rho})U_\rho^\dagger(x + \hat{\sigma})U_\sigma^\dagger(x), \\ P_{\rho\sigma}(x) &= U_{\rho\sigma}(x) + U_{\sigma,-\rho}(x) + U_{-\rho,-\sigma}(x) + U_{-\sigma,\rho}(x), \\ F'_{\rho\sigma}(x) &= \frac{1}{8} [P_{\rho\sigma}(x) - P_{\rho\sigma}^\dagger(x)], \\ F_{\rho\sigma}(x) &= -i \left[F'_{\rho\sigma}(x) - \frac{\text{Tr}^c F'_{\rho\sigma}(x)}{N_c} I \right], \end{aligned} \quad (\text{E2})$$

where Tr^c denotes the trace in the color space. To construct the flowed operator $F_{\rho\sigma}(t_f, x)$ at positive flow time t_f , all gauge links $U_\rho(x)$ are replaced by their flowed counterparts generated through the gradient flow.

Appendix F: Fitting strategies for ground-state matrix elements extraction from three-point functions

To extract the matrix elements of the quark or gluon EMT, we analyze the ratio of 3pt to 2pt correlation functions constructed using flowed EMT operators. This ratio is defined as

$$R_{X,\Gamma}^{\rho\sigma}(t,\tau) = \frac{C_{X,\Gamma}^{\rho\sigma}(t,\tau)}{C_\Gamma^{2\text{pt}}(t)}, \quad (\text{F1})$$

where $C_{X,\Gamma}^{\rho\sigma}(t,\tau)$ and $C_\Gamma^{2\text{pt}}(t)$ denote the three- and two-point functions respectively with $X = q, g$. Γ specifies the Dirac structure of the interpolating operator for the external meson state.

The three-point function admits the spectral decomposition:

$$C_{X,\Gamma}^{\rho\sigma}(t,\tau) = \sum_{m,n} Z_m^* Z_n \frac{\langle m | \tilde{\mathcal{O}}_{i,\rho\sigma} | n \rangle}{2M} e^{-\tau E_n} e^{-(t-\tau)E_m}. \quad (\text{F2})$$

Here, M represent the meson mass, while Z_n and E_n are the overlap amplitudes and energy levels of the meson states, which are identical to those appearing in the two-point function decomposition. $\langle 0 | \tilde{\mathcal{O}}_{i,\rho\sigma} | 0 \rangle / 2M$ is the target matrix element in the ground-state limit.

To reliably isolate ground-state contributions at finite time separations, we employ both two-state and summation fitting strategies. All fits are fully correlated, utilizing covariance matrices estimated via bootstrap resampling. The fit window for the operator insertion time τ is restricted to the interval $\tau \in [aN_{\text{skip}}, t - aN_{\text{skip}}]$, where the skip factor N_{skip} is chosen as

$$N_{\text{skip}} = \text{int}(\sqrt{8t_f}/a) + N_{\text{side}}, \quad (\text{F3})$$

where t_f denotes the gradient flow time and $N_{\text{side}} \in [6, 12]$ depends on the lattice spacing and fit strategy. This choice reflects the fact that gradient flow smears the operator over a radius $\sqrt{8t_f}$, which limits the temporal region where the flowed operator can reliably probe hadronic structure. A larger t_f reduces the usable fit range and simultaneously worsens the condition number of the covariance matrix. Therefore, when t_f is small, more (t, τ) data points are retained to improve the fit signal, while for large t_f , more points are discarded near the boundaries to ensure numerical stability.

To further reduce correlations among nearby (t, τ) values, we introduce a stride in both t and τ selection. For example, a stride of 2 uses separation $t/a = 28, 30, 32$ for quark and $t/a = 26, 28, 30$ for gluon, and insertion times $\tau/a = N_{\text{skip}}, N_{\text{skip}} + 2, N_{\text{skip}} + 4, \dots$. We perform two variants of the two-state fit, using stride-2 and stride-4 samples, denoted as Fit_{str2} and Fit_{str4} , respectively.

In the spectral decomposition of Eq. (F2), we truncate the sum to the lowest two states ($m, n = 0, 1$) and neglect the $m = n = 1$ term, which is exponentially suppressed for large t . The resulting two-state ansatz for the ratio takes the form

$$R_{X,\Gamma}^{\rho\sigma}(t, \tau) = \frac{1}{2M} \frac{\langle 0 | \tilde{\mathcal{O}}_{i,\rho\sigma} | 0 \rangle - \frac{\text{Re}(Z_1^* Z_0 \langle 0 | \tilde{\mathcal{O}}_{i,\rho\sigma} | 1 \rangle)}{|Z_0|^2} [e^{-\Delta E \tau} + e^{-\Delta E(t-\tau)}]}{1 + (|Z_1|^2 / |Z_0|^2) e^{-\Delta E t}}. \quad (\text{F4})$$

Since the external interpolating operators are the same in both two-point and three-point functions, we first analyze two-point functions to determine Z_n and E_n of each bootstrap sample, and then use them as fixed inputs in the analysis of the three-point function ratios.

We also apply the summation fit by adding the ratios over τ :

$$R_{X,\Gamma}^{\rho\sigma, \text{sum}}(t) = \sum_{\tau=aN_{\text{skip}}}^{t-aN_{\text{skip}}} R_{X,\Gamma}^{\rho\sigma}(t, \tau). \quad (\text{F5})$$

In large- t , this approximates

$$R_{X,\Gamma}^{\rho\sigma, \text{sum}}(t) = \frac{\langle 0 | \tilde{\mathcal{O}}_{i,\rho\sigma} | 0 \rangle}{2M} \cdot t + B, \quad (\text{F6})$$

where the slope directly yields the ground-state matrix element. We denote this method by SUM.

We perform 600 bootstrap samples for each parameter set $(\Gamma, a, t_f, \tilde{\mathcal{O}}_{i,\rho\sigma})$, and apply all three fitting strategies (Fit_{str2} , Fit_{str4} , and SUM), resulting in 1800 fits per observable. All results are collected into an extended bootstrap ensemble to capture both statistical and fit-related systematic uncertainties.

Appendix G: Extraction of EMT matrix elements for the η_c meson

For the pseudoscalar η_c , we choose $\Gamma = \gamma_5$ in the meson interpolator for the three-point functions defined in Equation D1 and Equation E1. In the asymptotic limit $t \gg \tau \gg 0$, the temporal and spatial components of the ratios approach

$$\begin{aligned} \frac{1}{2M} \langle \eta_c | \tilde{\mathcal{O}}_{3,44} | \eta_c \rangle &= \lim_{t \gg \tau \gg 0} R_{q,\gamma_5}^{44}, \\ \frac{1}{3} \sum_{k=1}^3 \frac{1}{2M} \langle \eta_c | \tilde{\mathcal{O}}_{3,kk} | \eta_c \rangle &= \lim_{t \gg \tau \gg 0} \frac{1}{3} \sum_{k=1}^3 R_{q,\gamma_5}^{kk}, \end{aligned} \quad (\text{G1})$$

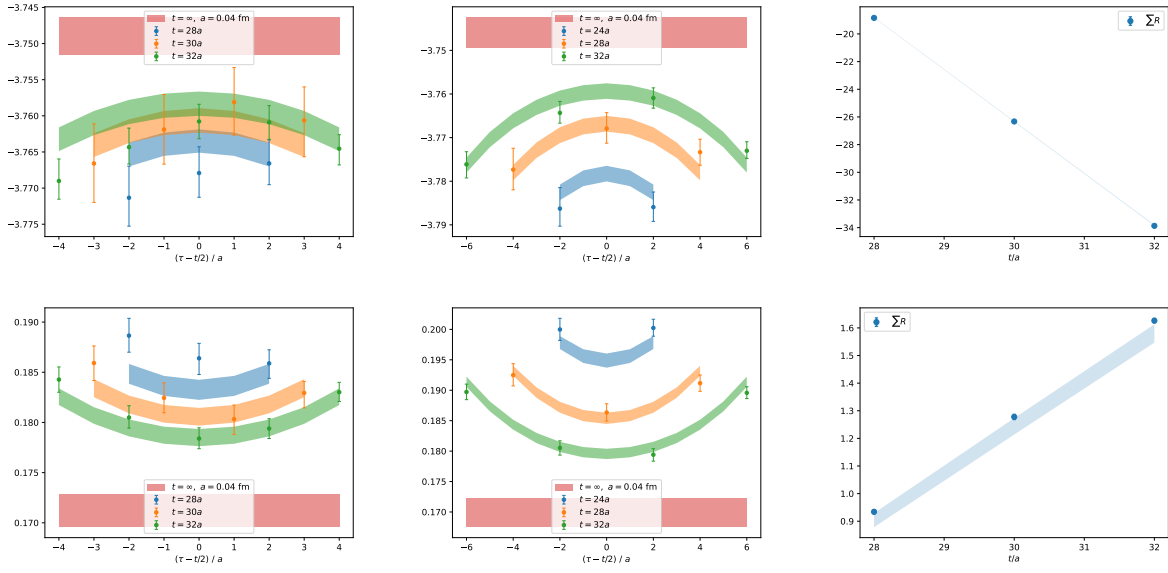


FIG. 5. Left and middle panels: ratios of quark three-point to two-point correlation functions for the η_c meson of $a = 0.04$ fm lattice at flow time $t_f = 5\epsilon_f$, plotted as functions of $t - \tau/2$. The curved bands represent reconstructions from the two-state fits $\text{Fit}_{\text{str}2}$ and $\text{Fit}_{\text{str}4}$, while the horizontal bands indicate the extracted ground-state matrix elements. Right panels: Summed ratios as functions of the source-sink separation t , with curved bands representing results from the summation fit SUM. The upper and lower rows show results for temporal components R_{q,γ_5}^{44} and spatial components $\sum_{k=1}^3 R_{q,\gamma_5}^{kk}/3$ respectively.

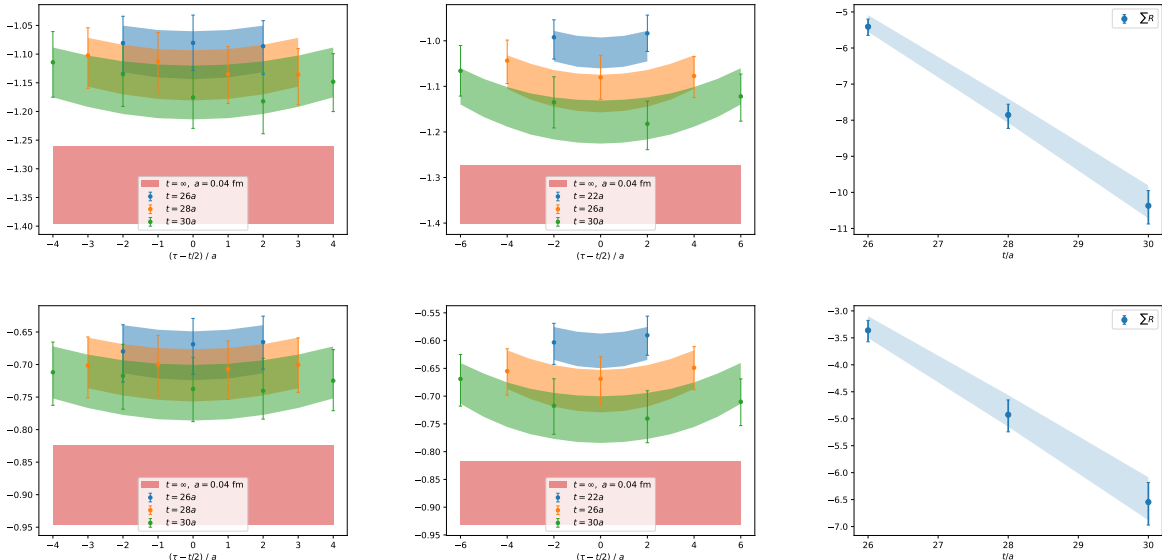


FIG. 6. Similar figures as Figure 5 but for gluonic matrix elements of η_c : R_{g,γ_5}^{44} (upper row) and $\sum_{k=1}^3 R_{g,\gamma_5}^{kk}/3$ (lower row).

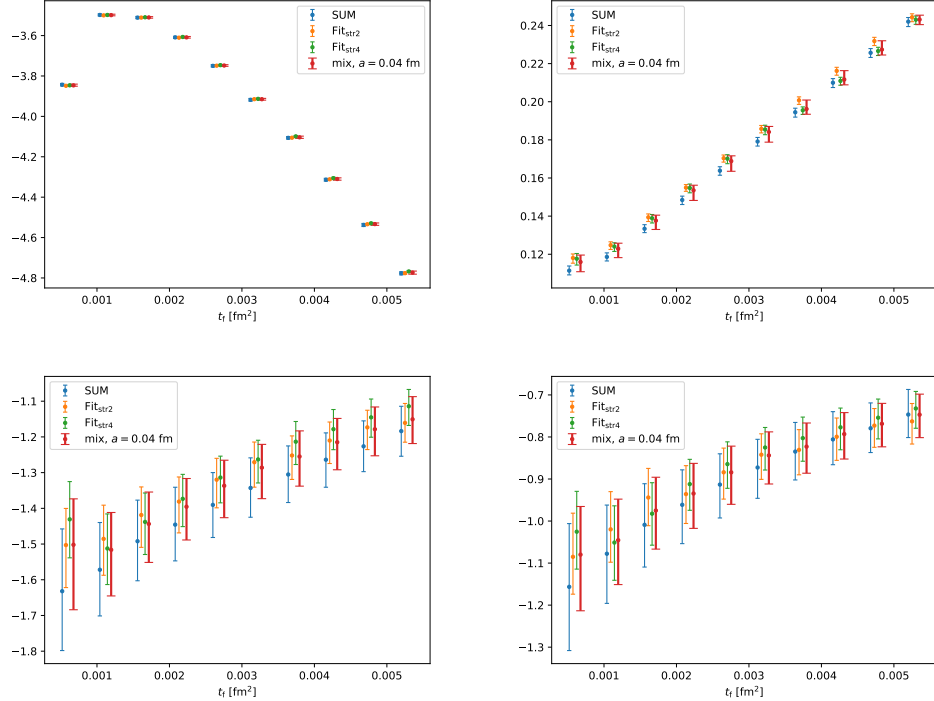


FIG. 7. Extracted EMT matrix elements for η_c from the summation fit SUM and two two-state fits Fit_{str2} and Fit_{str4} are shown as a function of flow time t_f . The averaged results are also shown (denoted by mix). The upper panels show quark matrix elements $\frac{1}{2M}\langle\eta_c|\tilde{\mathcal{O}}_{3,44}|\eta_c\rangle$ (left) and $\frac{1}{2M}\sum_{k=1}^3\langle\eta_c|\tilde{\mathcal{O}}_{3,kk}|3|\eta_c\rangle$ (right). The low panels show gluon matrix elements $\frac{1}{2M}\langle\eta_c|\tilde{\mathcal{O}}_{1,44}|\eta_c\rangle$ (left) and $\frac{1}{2M}\sum_{k=1}^3\langle\eta_c|\tilde{\mathcal{O}}_{1,kk}|3|\eta_c\rangle$ (right).

for the quark sector, and

$$\begin{aligned} \frac{1}{2M}\langle\eta_c|\tilde{\mathcal{O}}_{1,44}|\eta_c\rangle &= \lim_{t \gg \tau \gg 0} R_{g,\gamma_5}^{44}, \\ \frac{1}{3}\sum_{k=1}^3\frac{1}{2M}\langle\eta_c|\tilde{\mathcal{O}}_{1,kk}|\eta_c\rangle &= \lim_{t \gg \tau \gg 0} \frac{1}{3}\sum_{k=1}^3 R_{g,\gamma_5}^{kk}, \end{aligned} \quad (G2)$$

for the gluon sector, where $k = 1, 2, 3$ label spatial directions. In practice, we average the spatial components in the rest frame to improve statistical precision.

Figure 5 and Figure 6 show the extraction of the η_c quark and gluon EMT matrix elements on the $a = 0.04$ fm ensemble at $t_f = 5\epsilon_f$ respectively, for the temporal components R_{X,γ_5}^{44} (upper rows) and the averaged spatial components $\sum_{k=1}^3 R_{X,\gamma_5}^{kk}/3$ (lower rows), with $X = q, g$. In the left and middle panels, the three-point to two-point ratios are plotted as functions of $t - \tau/2$. The reconstructed curves from the two-state fits, Fit_{str2} and Fit_{str4}, track the data well over the full range of source–sink separations, indicating good control of excited-state contamination; the corresponding ground-state matrix elements are shown as horizontal bands. The right panels display the summed ratios versus t , where the SUM bands exhibit a clear linear behavior, consistent with the expected suppression of excited-state effects.

The extracted ground-state matrix elements from Fit_{str2}, Fit_{str4}, and SUM are summarized in Figure 7 as functions of the flow time t_f for the same $a = 0.04$ fm ensemble (upper

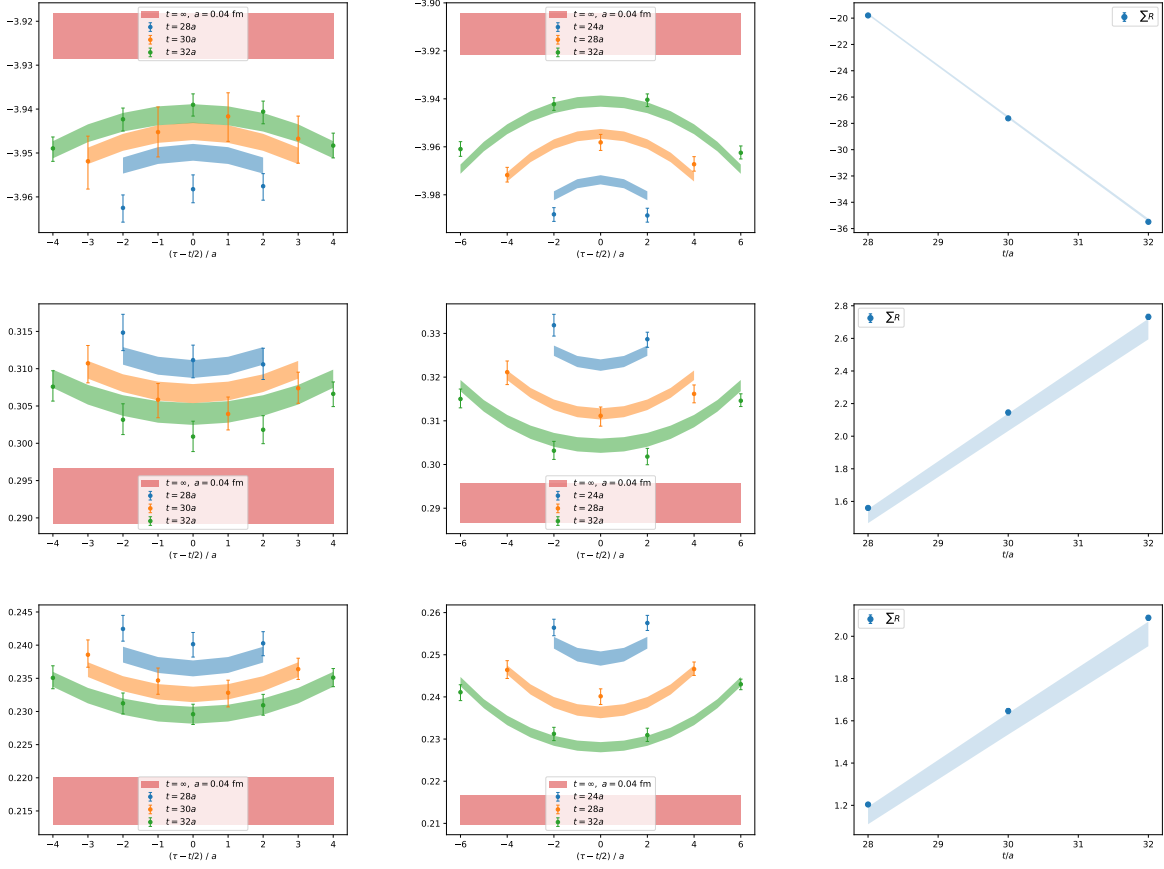


FIG. 8. Left and middle panels: Quark three-point to two-point function ratios for the J/ψ meson as functions of $t - \tau/2$, for the temporal (R_{q,γ_1}^{44} , first row), longitudinal (R_{q,γ_1}^{11} , second row), and transverse ($(R_{q,\gamma_1}^{22} + R_{q,\gamma_1}^{33})/2$, third row) components. Curved bands correspond to the two-state fits $\text{Fit}_{\text{str}2}$ and $\text{Fit}_{\text{str}4}$; horizontal bands indicate the extracted matrix elements. Right panels: Summed ratios plotted as functions of t , with straight bands from the summation fit SUM.

panels for quarks and lower panels for gluons). The three strategies yield mutually consistent results within statistical uncertainties across the t_f range, demonstrating the stability of the extraction with respect to both the excited-state treatment and the fit method. We also show the averaged results obtained by combining all $3 \times 600 = 1800$ bootstrap samples (labeled “mix”), which are used in the subsequent analysis.

Appendix H: Extraction of EMT matrix elements for the J/ψ meson

For the vector J/ψ channel we consider polarization along the x direction and use the interpolating operator $\Gamma = \gamma_1$. In the rest frame, the relevant quark EMT matrix elements

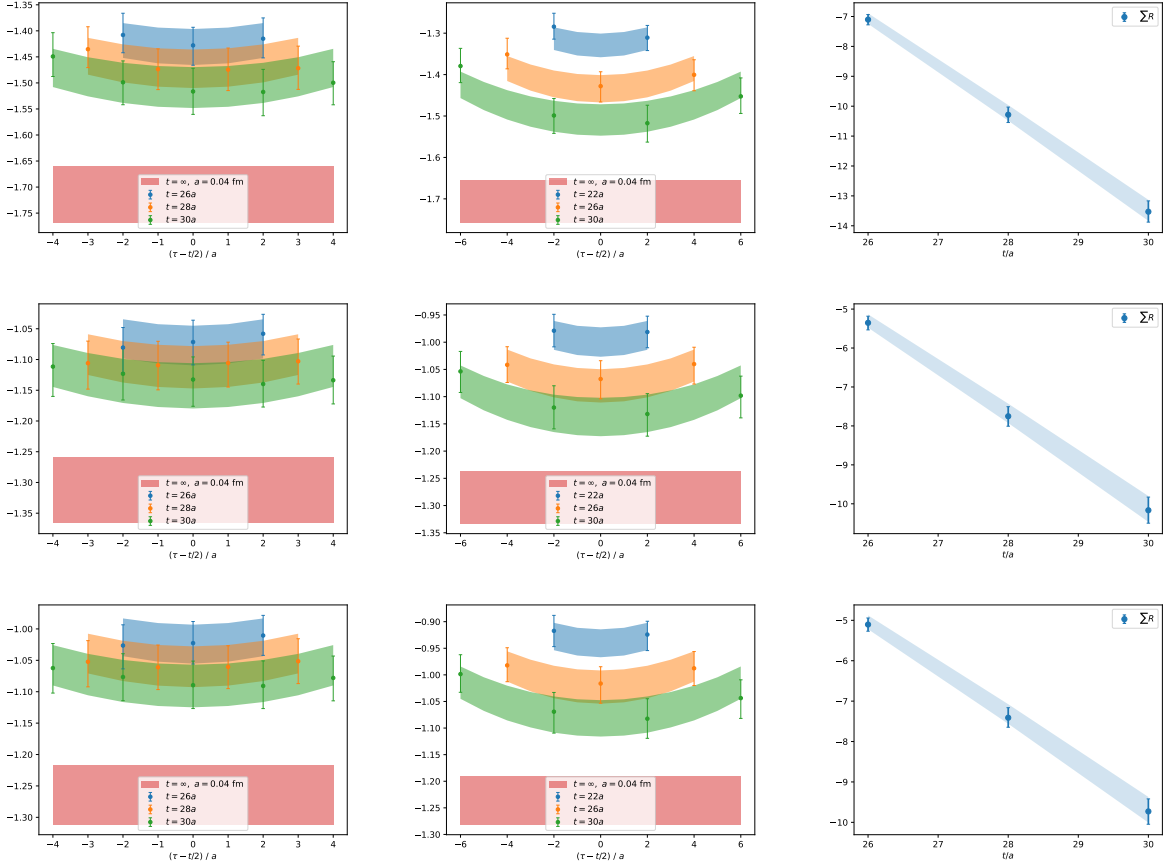


FIG. 9. Similar figures as Figure 8 but for gluonic matrix elements of J/ψ : $\frac{1}{3} \sum_{\lambda=1}^3 R_{g,\gamma_\lambda}^{44}$ (first row), $\frac{1}{3} \sum_{\lambda=1}^3 R_{g,\gamma_\lambda}^{\lambda\lambda}$ (second row) and $\frac{1}{6} \sum_{\lambda=1}^3 \sum_{k \neq \lambda} R_{g,\gamma_\lambda}^{kk}$ (third row).

are obtained from the ground-state limits of the ratios,

$$\begin{aligned}
 \frac{1}{2M} \langle J/\psi, \gamma_1 | \tilde{\mathcal{O}}_{3,44} | J/\psi, \gamma_1 \rangle &= \lim_{t \gg \tau \gg 0} R_{q,\gamma_1}^{44}, \\
 \frac{1}{2M} \langle J/\psi, \gamma_1 | \tilde{\mathcal{O}}_{3,11} | J/\psi, \gamma_1 \rangle &= \lim_{t \gg \tau \gg 0} R_{q,\gamma_1}^{11}, \\
 \frac{1}{2M} \left\langle J/\psi, \gamma_1 \left| \frac{\tilde{\mathcal{O}}_{3,22} + \tilde{\mathcal{O}}_{3,33}}{2} \right| J/\psi, \gamma_1 \right\rangle &= \lim_{t \gg \tau \gg 0} \frac{R_{q,\gamma_1}^{22} + R_{q,\gamma_1}^{33}}{2},
 \end{aligned} \tag{H1}$$

where the indices $k = 2, 3$ are transverse to the polarization direction. As in the pseudoscalar case, we average over the degenerate transverse components to improve statistical precision.

Figure 8 summarizes the quark-channel extraction for the $a = 0.04$ fm ensemble at $t_f = 5\epsilon_f$. The left and middle columns show the ratios R_{q,γ_1}^{44} (upper row), R_{q,γ_1}^{11} (middle row), and $(R_{q,\gamma_1}^{22} + R_{q,\gamma_1}^{33})/2$ (lower row) as functions of $t - \tau/2$, together with the reconstructed curves from the two-state fits using Fit_{str2} and Fit_{str4} . The fit reconstructions track the data well across the full range of source-sink separations, indicating robust isolation of the ground-state signal in all three channels. The right column displays the summed ratios versus t and the corresponding summation fits; the observed linear behavior provides an independent check that excited-state effects are suppressed. In Figure 10, we compare the

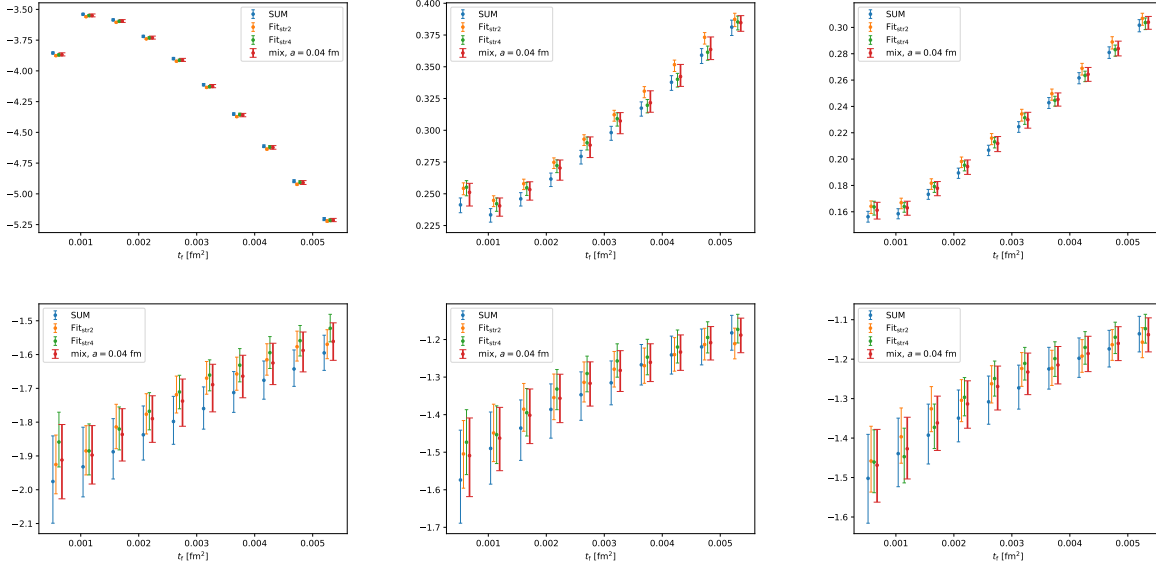


FIG. 10. Extracted EMT matrix elements for J/ψ from the summation fit SUM and two two-state fits $\text{Fit}_{\text{str}2}$ and $\text{Fit}_{\text{str}4}$ are shown as a function of flow time t_f . The averaged results are also shown (denoted by mix). The upper panels show quark matrix elements $\frac{1}{2M} \langle J/\psi, \gamma_1 | \tilde{\mathcal{O}}_{3,44} | J/\psi, \gamma_1 \rangle$ (left), $\frac{1}{2M} \langle J/\psi, \gamma_1 | \tilde{\mathcal{O}}_{3,11} | J/\psi, \gamma_1 \rangle$ (middle) and $\frac{1}{2M} \langle J/\psi, \gamma_1 | (\tilde{\mathcal{O}}_{3,22} + \tilde{\mathcal{O}}_{3,33})/2 | J/\psi, \gamma_1 \rangle$ (right). The low panels show gluon matrix elements $\frac{1}{2M} \langle J/\psi, \gamma_1 | \tilde{\mathcal{O}}_{1,44} | J/\psi, \gamma_1 \rangle$ (left), $\frac{1}{2M} \langle J/\psi, \gamma_1 | \tilde{\mathcal{O}}_{1,11} | J/\psi, \gamma_1 \rangle$ (middle) and $\frac{1}{2M} \langle J/\psi, \gamma_1 | (\tilde{\mathcal{O}}_{1,22} + \tilde{\mathcal{O}}_{1,33})/2 | J/\psi, \gamma_1 \rangle$ (right).

extracted ground-state matrix elements as functions of t_f for $\text{Fit}_{\text{str}2}$, $\text{Fit}_{\text{str}4}$ and SUM in the upper panels, which agree within uncertainties.

For the gluon EMT matrix elements we average over the three polarization directions $\lambda = 1, 2, 3$ with $\Gamma = \gamma_\lambda$, and use rotational symmetry to improve statistics. The corresponding relations in the rest frame are

$$\begin{aligned}
 \frac{1}{2M} \langle J/\psi, \gamma_1 | \tilde{\mathcal{O}}_{1,44} | J/\psi, \gamma_1 \rangle &= \lim_{t \gg \tau \gg 0} \frac{1}{3} \sum_{\lambda=1}^3 R_{g,\gamma_\lambda}^{44}, \\
 \frac{1}{2M} \langle J/\psi, \gamma_1 | \tilde{\mathcal{O}}_{1,11} | J/\psi, \gamma_1 \rangle &= \lim_{t \gg \tau \gg 0} \frac{1}{3} \sum_{\lambda=1}^3 R_{g,\gamma_\lambda}^{\lambda\lambda}, \\
 \frac{1}{2M} \left\langle J/\psi, \gamma_1 \left| \frac{\tilde{\mathcal{O}}_{1,22} + \tilde{\mathcal{O}}_{1,33}}{2} \right| J/\psi, \gamma_1 \right\rangle &= \lim_{t \gg \tau \gg 0} \frac{1}{6} \sum_{\lambda=1}^3 \sum_{k \neq \lambda} R_{g,\gamma_\lambda}^{kk},
 \end{aligned} \tag{H2}$$

where $k \neq \lambda$ denotes EMT components transverse to the polarization direction. Since $\lambda = 1, 2, 3$ are equivalent, on the left-hand side we display the γ_1 case for brevity.

Figure 9 presents the corresponding gluon-channel analysis. The left and middle columns show the ratios and the reconstructed curves from the two-state fits, the right panels display the summed ratios and summation fits. The lower panels of Figure 10 compile the resulting gluon matrix elements versus t_f from $\text{Fit}_{\text{str}2}$, $\text{Fit}_{\text{str}4}$, and SUM. The consistency among these extraction strategies provides a cross-check of excited-state control and systematic stability in the gluon channel.

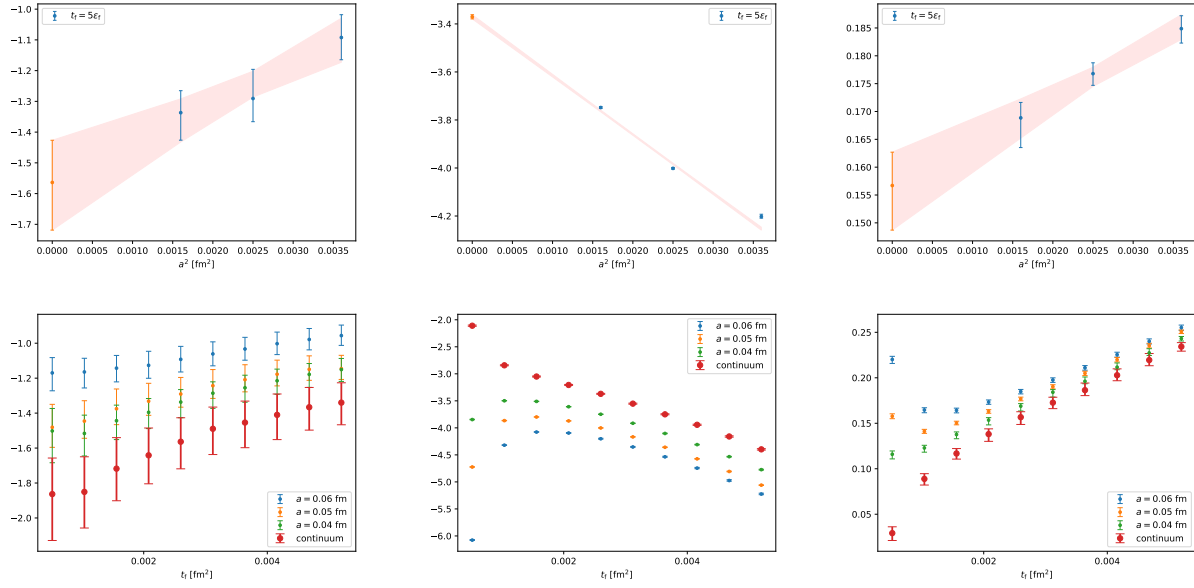


FIG. 11. Continuum extrapolation of selected gluon and quark EMT matrix elements in the η_c channel. Left: Temporal component of the gluon EMT, $\frac{1}{2M}\langle\eta_c|\tilde{\mathcal{O}}_{1,44}|\eta_c\rangle$. Middle: Temporal component of the quark EMT, $\frac{1}{2M}\langle\eta_c|\tilde{\mathcal{O}}_{3,44}|\eta_c\rangle$. Right: Spatial component of the quark EMT, $\frac{1}{2M}\langle\eta_c|\tilde{\mathcal{O}}_{3,kk}/3|\eta_c\rangle$. Top row displays the continuum extrapolation at flow time $t_f = 5\epsilon_f$. Bottom row shows the matrix elements at three lattice spacings and the continuum values as functions of flow time t_f .

Appendix I: Continuum extrapolation

The flowed matrix elements extracted from the ratio fits are still affected by lattice discretization errors [52]. Based on the lattice actions and operator constructions used in this study, the dominant discretization effects are of order $O(a^2)$. To obtain the continuum limit of the flowed matrix elements, we perform extrapolations in the lattice spacing a at fixed flow time t_f .

For each matrix elements $\langle H|\tilde{\mathcal{O}}_{i,\rho\sigma}|H\rangle$, and for each flow time t_f , we have 1800 bootstrap samples constructed from the combination of three fitting methods (Fit_{str2}, Fit_{str4}, and SUM) across multiple source-sink separations and multiple ensembles. Then at fixed flow time t_f , we apply the quadratic continuum extrapolation in a^2 sample by sample,

$$\langle H|\tilde{\mathcal{O}}_{i,\rho\sigma}|H\rangle(t_f, a) = \langle H|\tilde{\mathcal{O}}_{i,\rho\sigma}|H\rangle(t_f, 0) + a^2 X_{i,\rho\sigma}(t_f). \quad (I1)$$

Examples of the continuum extrapolation behavior are illustrated in Figure 11 for the η_c channel and Figure 12 for the J/ψ channel. The upper panels show representative examples of continuum extrapolations at $t_f = 5\epsilon_f$, where a clear linear dependence on a^2 is observed, supporting the validity of the extrapolation ansatz. In the lower panels, we present the continuum-extrapolated results as a function of t_f . As t_f decreases, statistical uncertainties increase due to reduced signal and stronger sensitivity to lattice artifacts. These findings underscore the importance of multi-ensemble analysis, particularly when working with gradient-flow-smeared operators.

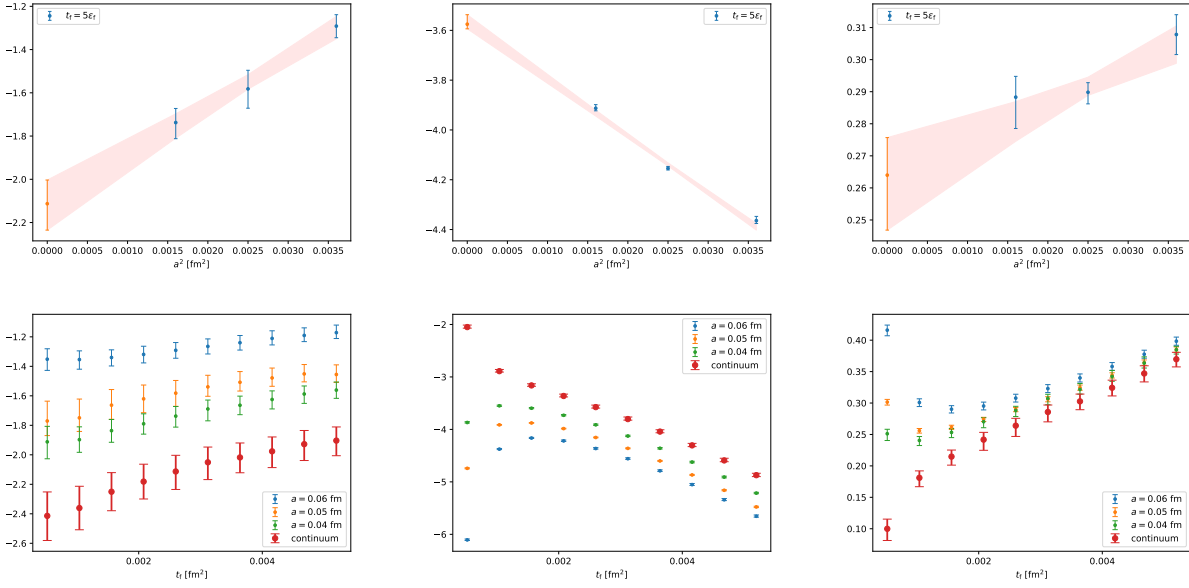


FIG. 12. The same as Figure 11 but for $\frac{1}{2M}\langle J/\psi, \gamma_1 | \tilde{\mathcal{O}}_{1,44} | J/\psi, \gamma_1 \rangle$, $\frac{1}{2M}\langle J/\psi, \gamma_1 | \tilde{\mathcal{O}}_{3,44} | J/\psi, \gamma_1 \rangle$, $\frac{1}{2M}\langle J/\psi, \gamma_1 | \tilde{\mathcal{O}}_{3,11} | J/\psi, \gamma_1 \rangle$.

Appendix J: Perturbative matching to $\overline{\text{MS}}$ scheme

The flowed EMT operator can be related to the renormalized EMT in the $\overline{\text{MS}}$ scheme through a perturbative matching procedure. Specifically, in the small flow-time limit, the flowed operator $\tilde{\mathcal{O}}_{i,\rho\sigma}(t_f)$ can be expanded in terms of renormalized local operators through,

$$\mathcal{O}_i^{\overline{\text{MS}}}(\mu) = M_{ij}(t_f, \mu) \tilde{\mathcal{O}}_j(t_f) + O(t_f), \quad (\text{J1})$$

with power corrections denoted by $O(t_f)$. The matching matrix $M_{ij}(t_f, \mu)$ is given by [58]

$$M_{ij}(t_f, \mu) = Z_{il}(\mu) [\zeta^{-1}]_{lj}(t_f, \mu), \quad (\text{J2})$$

where $[\zeta^{-1}]_{lj}(t_f, \mu)$ denotes the inverse matching from the flowed operator to the bare EMT operator in dimensional regularization and $Z_{il}(\mu)$ is the renormalization matrix in the $\overline{\text{MS}}$ scheme.

We apply the one-loop and two-loop results for M_{ij} computed in Ref. [58] to extract the renormalized operators $\mathcal{O}_{i,\rho\sigma}^{\overline{\text{MS}}}$, $i = 1, 2, 3, 4$, in the $\overline{\text{MS}}$ scheme.

Figure 13 shows examples of the matched matrix elements in the η_c channel after continuum extrapolation, comparing one-loop (blue) and two-loop (red) results for various operator components. The top row corresponds to the gluon sector, with the left and middle columns showing the temporal and spatial components of $\mathcal{O}_1^{\overline{\text{MS}}}$ respectively, and the right column displaying the gluon trace operator $\mathcal{O}_2^{\overline{\text{MS}}}$. The bottom row presents quark-sector results, including the temporal component $\mathcal{O}_{3,44}^{\overline{\text{MS}}}$, the averaged spatial components $\sum_{k=1}^3 \mathcal{O}_{3,kk}^{\overline{\text{MS}}} / 3$, and the quark trace operator.

We observe that the results obtained from one-loop and two-loop matching are generally close to each other, with only small differences. These differences are expected, as they

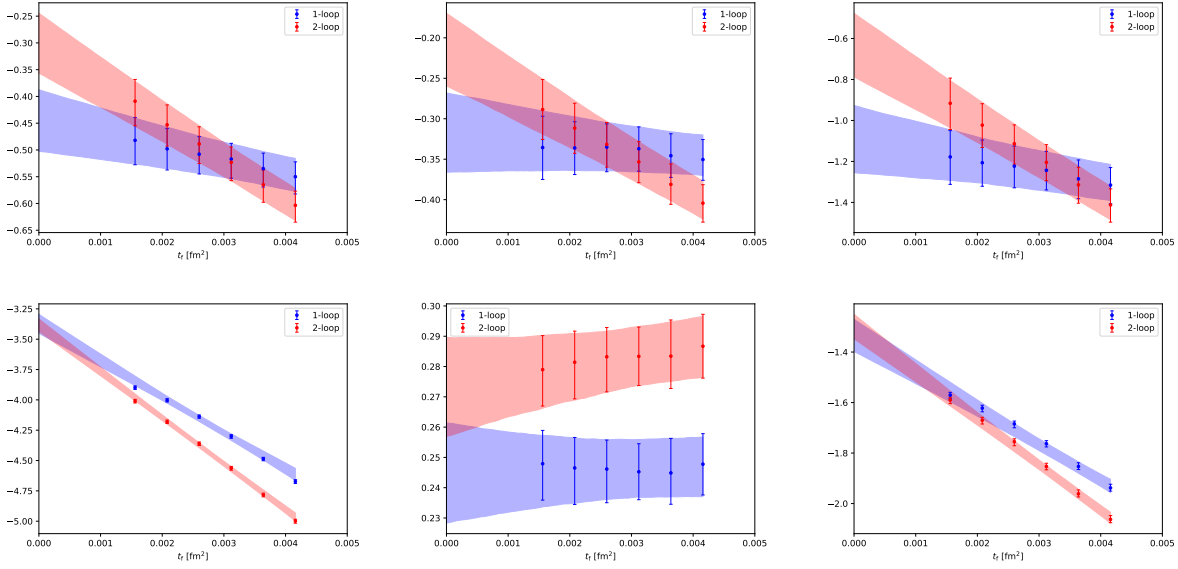


FIG. 13. Flow-time dependence of $\overline{\text{MS}}$ matrix elements in the η_c channel after continuum extrapolation and matching. Each panel compares results obtained using one-loop (blue) and two-loop (red) matching kernels. Top row (gluon sector): Left—Temporal component $\frac{1}{2M} \langle \eta_c | \mathcal{O}_{1,44}^{\overline{\text{MS}}} | \eta_c \rangle$; Middle—Averaged spatial components $\frac{1}{2M} \langle \eta_c | \mathcal{O}_{1,kk}^{\overline{\text{MS}}} / 3 | \eta_c \rangle$; Right—Trace component $\frac{1}{2M} \langle \eta_c | \mathcal{O}_{2,44}^{\overline{\text{MS}}} | \eta_c \rangle$. Bottom row (quark sector): Left—Temporal component $\frac{1}{2M} \langle \eta_c | \mathcal{O}_{3,44}^{\overline{\text{MS}}} | \eta_c \rangle$; Middle—Averaged spatial components $\frac{1}{2M} \langle \eta_c | \mathcal{O}_{3,kk}^{\overline{\text{MS}}} / 3 | \eta_c \rangle$; Right—Trace component $\frac{1}{2M} \langle \eta_c | \mathcal{O}_{4,44}^{\overline{\text{MS}}} | \eta_c \rangle$.

are of order $\mathcal{O}(\alpha_s^2)$. The small magnitude of the deviation also suggests that higher-order corrections beyond two loops are likely subdominant relative to our current statistical precision. This observation supports the robustness of the perturbative matching procedure and indicates that the conversion to the $\overline{\text{MS}}$ scheme is under good control within our error budget.

Appendix K: Small-flow time extrapolation

The gradient flow provides a theoretically clean method to define renormalized operators by smoothing ultraviolet fluctuations over a radius $\sqrt{8t_f}$ [49]. At positive flow time $t_f > 0$, composite operators constructed from flowed fields are finite and automatically renormalized. However, they are no longer identical to the original local QCD operators. Instead, they admit an operator product expansion (OPE) in flow time as indicated by Equation J2.

These $\mathcal{O}(t_f)$ terms arise because the flowed operator smears over a finite region, and therefore mixes with a tower of operators allowed by the symmetries. Such contamination cannot be removed by continuum or perturbative matching alone and must be explicitly eliminated via an extrapolation $t_f \rightarrow 0$. Only in this limit does the flowed matrix element reliably reproduce the target renormalized operator in the $\overline{\text{MS}}$ scheme.

To perform the extrapolation, we use the form:

$$\langle H | \mathcal{O}_{i,\rho\sigma}^{\overline{\text{MS}}} | H \rangle(\mu, t_f) = \langle H | \mathcal{O}_{i,\rho\sigma}^{\overline{\text{MS}}} | H \rangle(\mu) + Y_{i,\rho\sigma} t_f, \quad (\text{K1})$$

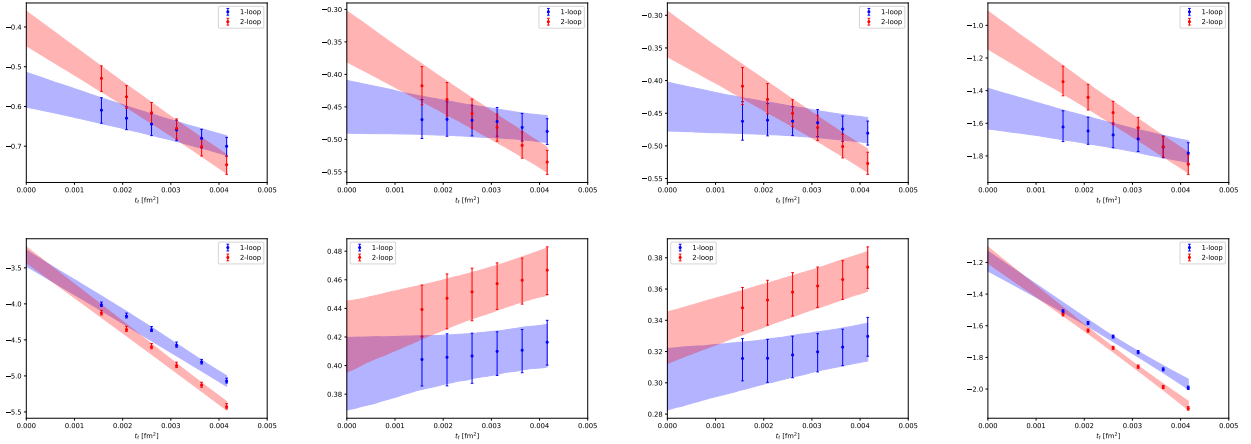


FIG. 14. Same as Figure 13 but for J/ψ . The upper row (left to right) shows the small- t_f extrapolations of gluon sector: $\frac{1}{2M} \langle J/\psi, \gamma_1 | \mathcal{O}_{1,44}^{\overline{\text{MS}}} | J/\psi, \gamma_1 \rangle$, $\frac{1}{2M} \langle J/\psi, \gamma_1 | \mathcal{O}_{1,11}^{\overline{\text{MS}}} | J/\psi, \gamma_1 \rangle$, $\frac{1}{2M} \langle J/\psi, \gamma_1 | (\mathcal{O}_{1,22}^{\overline{\text{MS}}} + \mathcal{O}_{1,33}^{\overline{\text{MS}}})/2 | J/\psi, \gamma_1 \rangle$, $\frac{1}{2M} \langle J/\psi, \gamma_1 | \mathcal{O}_{2,44}^{\overline{\text{MS}}} | J/\psi, \gamma_1 \rangle$. The lower row (left to right) shows the corresponding results of quark sector: $\frac{1}{2M} \langle J/\psi, \gamma_1 | \mathcal{O}_{3,44}^{\overline{\text{MS}}} | J/\psi, \gamma_1 \rangle$, $\frac{1}{2M} \langle J/\psi, \gamma_1 | \mathcal{O}_{3,11}^{\overline{\text{MS}}} | J/\psi, \gamma_1 \rangle$, $\frac{1}{2M} \langle J/\psi, \gamma_1 | (\mathcal{O}_{3,22}^{\overline{\text{MS}}} + \mathcal{O}_{3,33}^{\overline{\text{MS}}})/2 | J/\psi, \gamma_1 \rangle$, $\frac{1}{2M} \langle J/\psi, \gamma_1 | \mathcal{O}_{4,44}^{\overline{\text{MS}}} | J/\psi, \gamma_1 \rangle$.

and carry out a linear fit in t_f for each matrix element. To mitigate correlations between data at different flow times and reduce the condition number of the covariance matrix, we randomly select three t_f values from our available set for each of the 1800 bootstrap samples and perform an correlated linear fit. This procedure also allows us to estimate systematic uncertainties associated with the choice of fit window.

Examples of the flow-time extrapolation are shown in Figure 13 and Figure 14 for the η_c and J/ψ channels, respectively. The observed linear dependence indicates that higher-order flow-time corrections are negligible within our current precision. The extrapolated values thus represent the final results for EMT matrix elements in the $\overline{\text{MS}}$ scheme, with both statistical and systematic uncertainties properly propagated through the entire analysis pipeline.

Appendix L: Quark-line-disconnected contributions of the charm quark

In the main text, we computed the quark-sector matrix elements of the EMT using only the connected three-point diagrams, omitting the disconnected contributions. This choice was motivated by the expectation that, for the charm quark, disconnected diagrams are strongly suppressed and therefore make a negligible contribution to the total matrix element.

To verify this assumption, we explicitly evaluated the disconnected charm-quark contribution for $\frac{1}{2M} \langle \eta_c | \widetilde{\mathcal{O}}_{3,\rho\sigma} | \eta_c \rangle$ on the $a = 0.06$ fm ensemble. The results, shown in Figure 15, indicate that while the disconnected signal is nonzero with high statistical precision, it is tiny compared to the connected contribution shown in Figure 11, and well below the statistical uncertainties of the connected results.

This numerical check confirms that omitting disconnected diagrams in the charm-quark sector introduces a negligible systematic uncertainty at our current level of precision. Con-

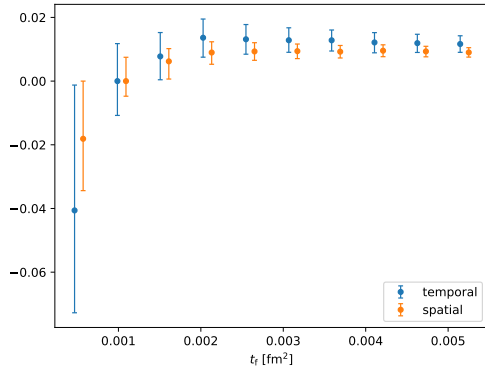


FIG. 15. The quark-line disconnected contribution to $\frac{1}{2M} \langle \eta_c | \tilde{\mathcal{O}}_{3,44} | \eta_c \rangle$ and $\frac{1}{2M} \langle \eta_c | \tilde{\mathcal{O}}_{3,kk/3} | \eta_c \rangle$ on the $a = 0.06$ fm ensemble.

sequently, restricting the calculation in main text to the connected contributions is fully justified for the present study.